

REVIEW OF LINEAR COLLIDER BEAM-BEAM INTERACTION*

PISIN CHEN

*Stanford Linear Accelerator Center,
Stanford, California 94309*

TABLE OF CONTENTS

ABSTRACT	2
1. INTRODUCTION	2
2. DISRUPTION EFFECTS	3
2.1 Luminosity Enhancement Without Offset	6
2.2 The Weak Focusing Regime	10
2.3 The Transition Regime	13
2.4 Pinch Confinement of Bunch Core	18
2.5 Luminosity Enhancement With Offset	26
2.6 Disruption Angles	28
2.7 Kink Instability	32
3. BEAMSTRAHLUNG EFFECTS	35
3.1 Energy Spectrum of Final Electrons	36
3.2 Maximum Deflection Angle	38
4. ELECTRON-POSITRON PAIR CREATION	40
4.1 Beamstrahlung Pair Creation	41
4.2 Energy Spectrum	43
4.3 Deflection Angle	45
REFERENCES	46

*Work supported by the Department of Energy, contract DE-AC03-76SF00515.

*Contributed to the U.S. Particle Accelerator School,
Batavia, Illinois, July 20-August 14, 1987*

ABSTRACT

Three major effects from the interaction of e^+e^- beams — disruption, beamstrahlung, and electron-positron pair creation — are reviewed. For the disruption effects we discuss the luminosity enhancement factor, the maximum and *rms* disruption angles, and the “kink instability”. All the results are obtained from computer simulations. Scaling laws for the numerical results and theoretical explanations of the computer acquired phenomena are offered wherever possible. For the beamstrahlung effects we concentrate only on the final electron energy spectrum resulting from multiple photon radiation process, and the deflection angle associated with low energy particles. For the effects from electron-positron pair creation, both coherent and incoherent processes of beamstrahlung pair creation are discussed. In addition to the estimation on total number of such pairs, we also look into the energy spectrum and the deflection angle.

1. INTRODUCTION

There are three major phenomena induced by the beam-beam interaction which are important to the design of high energy linear colliders. Namely, there is the *disruption* process where particle trajectories are bent by the collective EM field provided by the oncoming beam, and there is the *beamstrahlung* process where particles radiate due to the bending of the trajectories. The third major phenomenon, i.e., the *electron-positron pair creation*, is associated with the fact that during collision any high energy photon has a finite probability of turning itself into a e^+e^- pair with lower energy in general.

The most important impact of disruption is the deformation of the effective beam sizes during collision, which causes an enhancement on the luminosity. In addition, the disruption angle affects the constraints on the final quadrupole aperture. When the two beams are colliding with certain initial offset, the disruption effect between the two beams would induce a kink instability, which imposes a constraint on beam stability. Ironically, this instability helps to relax the offset tolerance for flat beams because the offset beams tend to find each other during the initial stage of the instability. Under a multi-bunch collision mode, however, the kink instability will largely degrade the luminosity through the relatively long growth time. On the other hand, the direct impact of beamstrahlung is the loss of the available energy for high energy events, and the degradation of beam energy resolution because of the stochastic nature of the radiation. Furthermore, the low

energy particles resulting either from beamstrahlung or from pair creation would be severely deflected by the strong beam-beam field, and would therefore impose constraints in the design of the linear collider interaction point region.

Most of the issues raised above can be studied by decoupling the disruption and the beamstrahlung effects. The energy loss due to beamstrahlung may modify the luminosity enhancement, but this effect can be ignored since we are only interested in the case where the average energy loss is small. Conversely, the average energy loss, the final energy spectrum and the pair creation process can be studied by assuming no disruption without compromising too much on accuracy. There is, however, one issue where the two effects are strongly coupled. This is the maximum disruption angle associated with the large deflections from the low energy particles.

In this lecture we review what has been studied on these issues. The computer simulations are performed using the code ABEL (Analysis of Beam-beam Effects in Linear colliders) described in Ref. 1, but improved considerably since it was first written. Although it is attempted to make this lecture pedagogical, many details are reluctantly omitted to avoid lengthiness. The reader is urged to consult the cited references in these circumstances.

2. DISRUPTION EFFECTS

It will be shown in this chapter that all the disruption effects can be well described by two Lorentz invariant parameters. Namely, one is the *disruption parameter* D , defined as

$$D_{x,y} = \frac{2r_e \sigma_z N}{\gamma \sigma_{x,y} (\sigma_x + \sigma_y)} \quad , \quad (2.1)$$

where r_e is the classical electron radius, γ the Lorentz factor of the relativistic beam, and $\sigma_x, \sigma_y, \sigma_z$ the *rms* beam size. Physically, D measures the strength of mutual focusing between the two beams. The other is the A parameter, defined as

$$A_{x,y} = \frac{\sigma_z}{\beta_{x,y}^*} \quad , \quad (2.2)$$

where $\beta_{x,y}$ are the β -functions at the interaction point of the e^+e^- beams.

Physically, A measures the inherent divergence of the incoming beam. This is important because the collision process takes place within several σ_z 's around the interaction point, and the natural variation of the beam size over such a distance due to the finiteness of the β -function would have significant impact on the disruption process. In the study of disruption effects one often chooses to fix the beam size σ_0 (for round beams) or σ_x and σ_y (for flat beams) at the interaction point so that the nominal luminosity (in the absence of disruption)

can be computed. In such case A is related to the invariant emittance ϵ_n via the relation $A = \epsilon_n \sigma_z / \gamma \sigma_0^2$. Furthermore, one can easily verify that A/D manifests the initial phase space area per particle of the beam in units of the classical electron radius:

$$\frac{A}{D} = \frac{\epsilon_n}{r_e N}, \quad (2.3)$$

which is independent of the optics that the beam experiences. Similar arguments also apply to flat beams.

In this lecture we assume the same initial parameters for the colliding electron and positron beams. The longitudinal coordinate s is fixed to the center-of-mass frame whose origin is the collision point of the two bunch centers. The time coordinate t is defined such that $t = 0$ when the two bunch centers collide. We further introduce the longitudinal coordinates z_j ($j = 1, 2$) co-moving with the two bunches. The origin of z_j is the center of the j th bunch, and z_j is positive along the direction of motion of the beam (see Fig. 1).

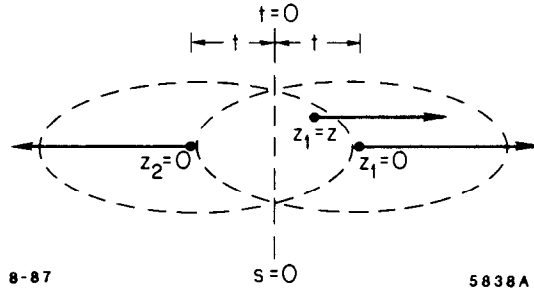


Fig. 1. Schematic diagram that defines the various coordinates of the two colliding bunches. For a test particle in bunch 1 at $z_1 = z$, the relative coordinate with respect to bunch 2 is $z_2 = -2t - z$.

In our calculations we shall ignore the longitudinal component of the focusing force, which is of the order $1/\gamma$ smaller than the transverse component. Thus the coordinate z_j of a particle is a constant in t . It is easy to see that particles in one

bunch that arrive at s at time t should have their co-moving coordinate z_1 related to s by

$$s = z_1 + t \quad . \quad (2.4)$$

where we adopt the convention that the speed of light $c = 1$. On the other hand, particles in the opposite bunch arriving at the same space-time point would have their co-moving coordinate z_2 related by

$$s = -z_2 - t \quad . \quad (2.5)$$

With these relations in mind, the luminosity for $A = 0$ is defined by

$$\mathcal{L} = 2fN^2 \int dx dy ds dt n_1(x, y, z_1, t) n_2(x, y, z_2, t) \quad . \quad (2.6)$$

where f is the repetition rate of collisions, and $n_j(x, y, z_j, t)$ the distribution function of the j th beam at time t , normalized such that

$$\int n_j(x, y, z_j, t) dx dy dz_j = 1 \quad . \quad j = 1, 2 \quad . \quad (2.7)$$

Since we ignore the longitudinal force, the longitudinal distributions are constant in time, i.e.,

$$\int n_j(x, y, z_j, t) dx dy = n_z(z_j) = \frac{1}{\sqrt{2\pi}\sigma_z} \exp \left\{ -\frac{z_j^2}{2\sigma_z^2} \right\} \quad . \quad (2.8)$$

In the absence of disruption, the luminosity in Eq. (2.6) can be straightforwardly integrated (assuming Gaussian distributions) to get

$$\mathcal{L}_0 = \frac{fN^2}{4\pi\sigma_0^2} \quad . \quad (2.9)$$

When $A \neq 0$, the above expression should be modified to take into account the variation of the beam cross section due to the change of the β -function around the interaction point. This can be done by introducing a reduction factor η_A :

$$\eta_A = \frac{2}{\sqrt{\pi}\sigma_z} \int_0^\infty \frac{e^{-z^2/\sigma_z^2}}{1 + z^2/\beta^{*2}} dz \quad , \quad (2.10)$$

such that the luminosity for a finite A in the absence of disruption is

$$\mathcal{L}_A = \eta_A \mathcal{L}_0 \quad . \quad (2.11)$$

Numerically, $\eta_A \simeq 0.76$ at $A = 1.0$, and rapidly approaches unity for $A < 1$. Since a reasonably designed accelerator would presumably be chosen to work in the regime where $A < 1$ to avoid degradation on luminosity, we find it convenient to use \mathcal{L}_0 as a reference parameter for all values of A .

When the disruption is included, the effective luminosity \mathcal{L} would be different from \mathcal{L}_0 , and a luminosity enhancement factor H_D is introduced to account for the change

$$H_D \equiv \frac{\mathcal{L}}{\mathcal{L}_0} \quad (2.12)$$

Note that with H_D so defined without η_A involved, it is possible that $H_D \lesssim 1$ when D is small but A is large.

By the same token, we introduce a disruption angle enhancement factor H_θ . In the weak focusing limit where $D \ll 1$, the approximate solution of the equation of motion for a particle with impact parameter r_0 can be shown to be

$$\left. \frac{dr}{dt} \right|_{final} \sim -\frac{r_e N}{\gamma \sigma_0^2} r_0 \quad (2.13)$$

Thus the nominal disruption angle can be defined as

$$\theta_0 = \frac{r_e N}{\gamma \sigma_0} = D \frac{\sigma_0}{\sigma_z} \quad (2.14)$$

The effective disruption angles θ_D for an arbitrary D is generally different from θ_0 , so H_θ is defined as

$$H_\theta \equiv \frac{\theta_D}{\theta_0} \quad (2.15)$$

2.1 Luminosity Enhancement Without Offset

Our primary interest is the enhancement of luminosity due to the mutual pinching of the two colliding beams. The details have been discussed in Ref. 2 for round beams and will be given in Ref. 3 for flat beams. As was pointed out in Ref. 2, the luminosity is infinite if the initial beam is paraxial and the computation is perfectly accurate. This is because a paraxial beam can be focused to a singular point. In reality, however, a beam will always have certain inherent divergence, and the singularity is only approached asymptotically. To account for this effect, as mentioned earlier, a parameter $A_{x,y} = \sigma_z / \beta_{x,y}^*$ is introduced,²⁾ which is proportional to the emittance for a given beam size $\sigma_{x,y}$. The computed enhancement factor $H_D = \mathcal{L} / \mathcal{L}_0$, where \mathcal{L}_0 is the geometrical luminosity without the effect of the depth of focus related to $A_{x,y}$ taken into account, is plotted in Fig. 2 as a function of D_y and A_y for flat beams.

The data in Fig. 2 are obtained by using a distribution function which is uniform in x and Gaussian in y and z (UGG), instead of a three-dimensional Gaussian distribution (GGG), for easiness of computation. The enhancement factor of GGG distributions for a given D_y can be deduced from a superposition

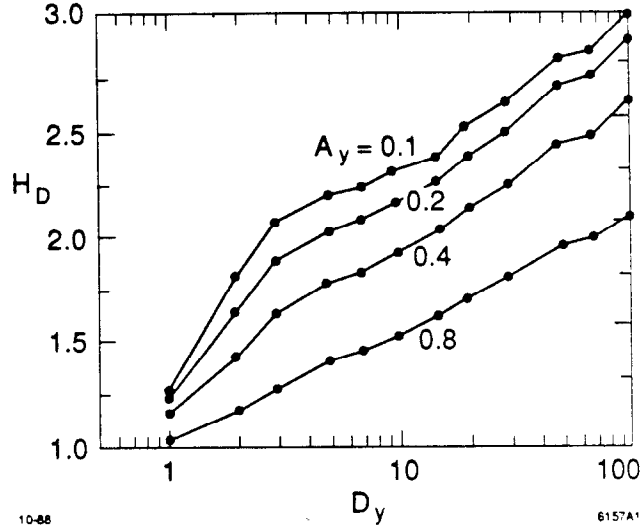


Fig. 2. Luminosity enhancement factor as a function of D_y , computed with four different values of A_y . The A_y values are so chosen that they are equally separated on the logarithmic scale.

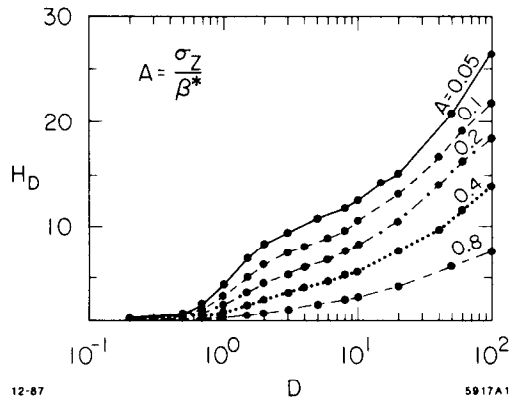


Fig. 3. Luminosity enhancement factor for round beams.

of UGG results with disruption parameters ranging from 0 near the horizontal edge to $\sqrt{6/\pi}D_y$ at the beam center. The enhancement factor for round beams is shown in Fig. 3.

By comparing Figs. 2 and 3, one finds that the enhancement factor for flat beams scales roughly as the cube-root of the corresponding value for round beams: which obeys the following empirical scaling law that fits all data points in Fig. 2

to within 10% accuracy:

$$H_D = 1 + D^{1/4} \left(\frac{D^3}{1 + D^3} \right) \left[\ln(\sqrt{D} + 1) + 2 \ln\left(\frac{0.8}{A}\right) \right] . \quad (2.1.1)$$

The reason for the flat beam enhancement not being scaled as a square root of the corresponding value for the round beam is because the horizontal focusing can enhance the vertical pinch effect (and vice versa) in the round beam case, whereas for flat beams the pinch in the major (horizontal) dimension can hardly affect the disruption in the minor dimension.

In both cases, the Chen-Yokoya results indicate a logarithmic divergence of H_D as a function of A , or A_y . In addition, H_D is monotonically increasing as a function of D , or D_y , at least up to $D = 100$. This second point is qualitatively the same as that found by Fawley and Lee⁴⁾ but in contradiction to Holebeek⁵⁾ and Solyak,⁶⁾ where the enhancement factor first saturates before eventually decreases at large D 's.

The difference appears to be due to the different ways of handling stochastic errors. In a Monte Carlo simulation the initial condition is generated by random numbers, which introduces a statistical fluctuation, and therefore an asymmetry, of the order $1/\sqrt{N_p}$, N_p being the number of macro particles. This asymmetry will be amplified during collision (i.e., kink instability) due to the beam-beam force, especially when the disruption parameter is large. The fact that the number of macro particles in a simulation is typically much smaller than the actual particle number, this fluctuation is artificially enhanced if no proper action is taken. To minimize this computation error in the study of luminosity enhancement without offset, the particle distribution function should be symmetrized at every time step in the calculation, so that the beam-beam force has the up-down symmetry at all times for the flat beam case. Similarly, in the round beam case only the radial force is computed. This process eliminates the possible instability triggered by computation errors.

The actual collisions are expected to have some unavoidable initial offset in alignment and skewness in distributions. This effect will be discussed in the next section.

In order to analyze the physical mechanism of the disruption process which give rise to the H_D behavior shown in Figs. 2 and 3, it is useful to investigate the time evolution of H_D . The differential luminosity (per unit time), $d\mathcal{L}/dt$, can be defined as

$$\frac{d\mathcal{L}}{dt} = 2f N^2 \int dx dy ds \, n_1(x, y, z_1, t) \, n_2(x, y, z_2, t) . \quad (2.1.2)$$

By the same token the differential luminosity enhancement factor, dH_D/dt , is defined by

$$\frac{dH_D}{dt} = \frac{1}{\mathcal{L}_0} \frac{d\mathcal{L}}{dt} , \quad (2.1.3)$$

such that

$$H_D = \int_{-\infty}^{\infty} \frac{dH_D}{dt} dt . \quad (2.1.4)$$

In the absence of disruption it is easy to see that

$$\frac{dH_D}{dt} = \frac{1}{\sqrt{2\pi} \sigma_z} \exp \left\{ \frac{-t^2}{\sigma_z^2} \right\} , \quad (2.1.5)$$

and from this expression $\int (dH_D/dt) dt = 1$, by definition. Figure 4 shows dH_D/dt as a function of time for various values of D for round beams. Silimar behavior is also seen for flat beams, though not as dramatic. Here the parameter A is fixed at 0.05, and the time t is in units of σ_z/c . In spite of the fact that the H_D curves in Fig. 3 are reasonably smooth for each fixed value of A , the curves shown in Fig. 4 reveals different characteristics throughout the entire range of the value of D .

For very small and very large D 's, dH_D/dt varies as a Gaussian function (although for large D regime there are small wiggles superimposed), while for medium values of D there is an obvious spike.

For very small D , e.g., $D \lesssim 0.6$, we find that dH_D/dt varies essentially as Eq. (2.1.5), which reflects the square of the longitudinal particle distribution of the bunch. When $D \sim 0.5$, a second peak appears at $t \simeq 1.6 \sigma_z/c$. The peak grows as D gets larger, and eventually becomes the dominant source for the luminosity enhancement by $D \simeq 0.7$. Notice also that the location of the second peak shifts gradually to the left as D increases, where the strong disruption induces the phenomena to occur earlier in time. Furthermore, while the buildup of the second peak becomes steeper, its falloff becomes smoother as D increases. This phenomena of a second peak appears in the region $0.5 \lesssim D \lesssim 5$. Beyond $D \sim 5$, the differential luminosity evolves into a new regime. The "second" peak now occurs right near the beginning of the collision, and its smooth *falloff* now recovers the Gaussian-like variation, except that there appear to be high-frequency wiggles superimposed. While the time evolution of dH_D/dt in both the small and the large D regimes behave similarly, their absolute values are distinctively different.

It turns out that the underlying physical mechanisms are indeed very different in the above mentioned three regimes of D , classified as follows: (1) the small D ($D \lesssim 0.5$), or the *weak focusing* regime, (2) the medium D ($0.5 \lesssim D \lesssim 5$), or the *transition* regime, and (3) the large D ($5 \lesssim D$), or the *pinch confinement*

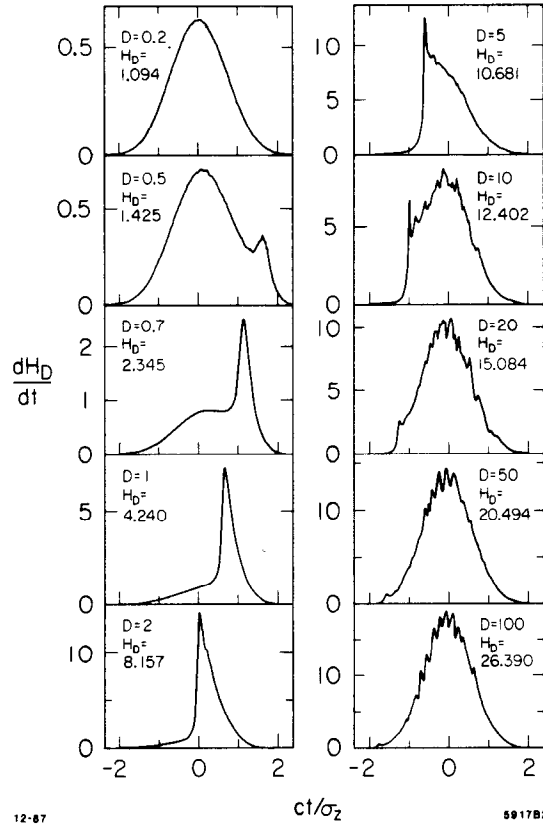


Fig. 4. Computer analysis on the time evolution of the luminosity enhancement factor H_D , at various different values of D with $A = 0.05$.

regime. In the following sections we shall provide theoretical descriptions that qualitatively explains the phenomena occurs in the three regimes.

2.2 The Weak Focusing Regime

The weak focusing regime corresponds to the range $0 < D \lesssim 0.5$. For such small values of D , dH_D/dt is essentially described by the Gaussian function in Eq. (2.1.5). The correction to this expression to the first order in D can be derived in the following way. For the sake of argument we assume $A = 0$. This is justified because it turns out that there is no divergence at $A = 0$ in the correction term linear in D , i.e., to this order the correction arises only through the radial motions of the particles.

The equation of motion of a particle at z_1 in a bunch is

$$\frac{d^2 r}{dt^2} = -\frac{4Nr_e}{\gamma} f_0(r) n_z(-2t - z_1), \quad (2.2.1)$$

with

$$f_0(r) \equiv \frac{1}{r} \int_0^r n_{r0}(r) r dr . \quad (2.2.2)$$

where $n_{r0}(r)$ is the unperturbed radial distribution function normalized such that $\int n_{r0}(r) r dr = 1$. To derive the first order correction we had assumed unperturbed distribution on the right-hand side of Eq. (2.2.1). The solution of Eq. (2.2.1) with initial conditions $r = r_0$, and $dr/dt = 0$ at $t = -\infty$ is given by

$$r(t, z_1) = r_0 - \frac{4Nr_e}{\gamma} f_0(r_0) g(t, z_1) , \quad (2.2.3)$$

with

$$g(t, z_1) = \int_{-\infty}^t dt_1 \int_{-\infty}^{t_1} dt_2 n_z(-2t_2 - z_1) = \int_{-\infty}^t dt_1 (t - t_1) n_z(-2t_1 - z_1) .$$

Equation (2.2.3) can be inverted as

$$r_0 \doteq r + \frac{4Nr_e}{\gamma} f_0(r) g(t, z_1) , \quad (2.2.4)$$

within the same order of accuracy. For our purpose we like to know the perturbed radial distribution function $n_r(r)$ at (t, z_1) . This can be found by

$$\begin{aligned} n_{r1}(r, t, z_1) &= n_{r0}(r_0) \frac{d(r_0^2)}{d(r^2)} \\ &= n_{r0}(r) \left[1 + \frac{4Nr_e}{\gamma} \left(\frac{1}{n_{r0}} \frac{dn_{r0}}{dr} f_0(r) + n_{r0} \right) g(t, z_1) \right] . \end{aligned} \quad (2.2.5)$$

Accordingly, the luminosity can be evaluated as

$$\begin{aligned} \mathcal{L} &\propto \int r dr dz_1 dz_2 n_z(z_1) n_z(z_2) \left[n_{r1}(r, t, z_1) n_{r1}(r, t, z_2) \right]_{t=-(z_1+z_2)/2} , \\ &= \int r dr dz_1 dz_2 n_z(z_1) n_z(z_2) [n_{r0}(r)]^2 \\ &\quad \times \left\{ 1 + \frac{4Nr_e}{\gamma} \left(\frac{1}{n_{r0}} \frac{dn_{r0}}{dr} f_0 + n_{r0} \right) \left[g(t, z_1) + g(t, z_2) \right] \right\}_{t=-(z_1+z_2)/2} , \end{aligned} \quad (2.2.6)$$

where the leading term (unity) corresponds to the nominal luminosity \mathcal{L}_0 . The integration over r can be carried out, which gives

$$\int_0^\infty r dr n_{r0}^2 \left(\frac{1}{n_{r0}} \frac{dn_{r0}}{dr} f_0 + n_{r0} \right) = \frac{1}{2} \int_0^\infty r dr n_{r0}^3 \quad (2.2.7)$$

Thus the luminosity enhancement factor for small D is

$$H_D \simeq 1 + \frac{4Nr_e}{\gamma} \left[\frac{\frac{1}{2} \int r dr n_{r0}^3}{\int r dr n_{r0}^2} \right] \times \int dz_1 dz_2 n_z(z_1) n_z(z_2) \left[g(t, z_1) + g(t, z_2) \right]_{t=-(z_1+z_2)/2} \quad (2.2.8)$$

Since the two colliding bunches are symmetric, $g(t, z_1)$ and $g(t, z_2)$ contribute equally to H_D , where

$$g(t, z_1) \Big|_{t=-(z_1+z_2)/2} = \int_{-\infty}^t dt_1 (t - t_1) n_z(-2t_1 - z_1) = \frac{1}{4} \int_0^\infty \tau d\tau n_z(\tau + z_2) \quad (2.2.9)$$

Therefore

$$H_D \simeq 1 + \frac{4Nr_e}{\gamma} \left[\frac{\int r dr n_{r0}^3}{\int r dr n_{r0}^2} \right] \iint dz_1 dz_2 n_z(z_1) n_z(z_2) \int_0^\infty \tau d\tau n_z(\tau + z_2) \\ = 1 + \frac{4Nr_e}{\gamma} \left[\frac{\int r dr n_{r0}^3}{\int r dr n_{r0}^2} \right] \int_0^\infty dz \int_0^\infty \tau d\tau n_z(z) n_z(\tau + z) \quad (2.2.10)$$

Now we introduce normalized coordinates $\rho = r/\sigma_0$, and $\zeta = z/\sigma_z$. Then

$$H_D = 1 + D \left[\frac{\int \rho d\rho n_{r0}^3}{\int \rho d\rho n_{r0}^2} \right] \int_0^\infty d\zeta \int_0^\infty \tau d\tau n_z(\zeta) n_z(\tau + \zeta) \quad (2.2.11)$$

For Gaussian and uniform distributions, this leads to

$$H_D = 1 + D \times \left\{ \begin{array}{l} \frac{2}{3} \text{ (radially Gaussian)} \\ \frac{1}{2} \text{ (radially uniform)} \end{array} \right\} \times \left\{ \begin{array}{l} \frac{1}{\sqrt{\pi}} \text{ (longitudinally Gaussian)} \\ \frac{1}{\sqrt{3}} \text{ (longitudinally uniform)} \end{array} \right\} \quad (2.2.12)$$

This formula agrees very well with the simulation results for $D \lesssim 0.6$. Notice that for $D \ll 1$, the empirical expression for H_D in Eq. (2.1.1) behaves as $D^{15/4}$, which is by no means close to the linear behavior in Eq. (2.2.12). This is mainly because of the need to suppress the strong $\ln(1/A)$ dependence in Eq. (2.1.1) in the small D regime. This strong $\ln(1/A)$ dependence, however, is necessary to fit the medium and large D regimes.

Rigorously speaking, H_D cannot be Taylor expanded around $D = 0$. In deriving Eq. (2.2.4) we have assumed that the first term r_0 on R.H.S. of Eq. (2.2.3) is much larger than the second term. This is not the case when t becomes large, no matter how small D is. One obvious example is that at the focal point the two terms would become equal. For $D \ll 1$, however, this focal point lies far beyond the tail of the oncoming bunch, thus the subtlety mentioned above is alleviated. To be more explicit, from linear optics it is easy to see that the focal length in the weak focusing regime is proportional to σ_z/D , thus the density of the oncoming beam around the focal point is proportional to $\exp\{-1/2 D^2\} \ll 1$. Since H_D comes from multiplication of the local densities of the two bunches, the contribution from the focal point is exponentially small.

2.3 The Transition Regime

The transition regime is characterized by the appearance of the second peak in dH_D/dt with relatively short duration. This phenomena also conforms with the fact that in this regime the first focal point lies inside the bulk of the oncoming beam. Because of the strong focusing, the deformation of the oncoming beam cannot be ignored. As we will show later in this section, the leading order correction in D for the target bunch deformation is equivalent to the second order contribution in D to the focusing force. To set the stage for the second order calculations, however, we shall still start with the first order approach where the equation of motion is given by Eq. (2.2.1). For small x in a Gaussian distribution we have

$$\begin{aligned} \frac{d^2 x}{dt^2} &= -\frac{4Nr_e}{\sqrt{2\pi}\gamma} \frac{x}{2\sigma_0^2\sigma_z} \exp\left\{-\frac{(2t+z_1)^2}{2\sigma_z^2}\right\} \\ &= -\frac{2D}{\sqrt{2\pi}} \frac{x}{\sigma_z^2} \exp\left\{-\frac{(2t+z_1)^2}{2\sigma_z^2}\right\} \end{aligned} \quad (2.3.1)$$

It suffices to solve the equation

$$\frac{d^2 x}{dt^2} = -\frac{2D}{\sqrt{2\pi}} \frac{x}{\sigma_z^2} \exp\left\{-\frac{2t^2}{\sigma_z^2}\right\}, \quad (2.3.2)$$

which arises from a coordinate transformation from t to $t + z_1/2$. Let us denote the two solutions to Eq. (2.3.2) by $u_1(t)$ and $u_2(t)$, with initial conditions at $t = -\infty$

$$u_1 = 1 + \mathcal{O}\left(\frac{1}{t}\right) \quad , \quad u_2 = t + \mathcal{O}\left(\frac{1}{t}\right) \quad , \quad (2.3.3)$$

respectively. We are interested in the solutions near the focal point, which for $D \lesssim 5$ occurs at $t_0 \sim \sigma_z/D$. By definition, at the focal point $u_1(t_0) = 0$. Numerical integration then gives the following approximate solution:

$$\dot{u}_1(t_0) \simeq -\frac{3}{4} \frac{\sqrt{D}}{\sigma_z} \quad , \quad (0.5 \lesssim D \lesssim 5) \quad , \quad (2.3.4)$$

while

$$u_2(t_0) = -\frac{1}{\dot{u}_1(t_0)} \simeq \frac{4}{3} \frac{\sigma_z}{\sqrt{D}} \quad , \quad (0.5 \lesssim D \lesssim 5) \quad . \quad (2.3.5)$$

The last relation comes from the Wronskian property:

$$u_1(t)\dot{u}_2(t) - \dot{u}_1(t)u_2(t) = 1 \quad . \quad (2.3.6)$$

The general solution to Eq. (2.3.2) is therefore

$$x = x_0 u_1(t) + x'_0 u_2(t) \quad . \quad (2.3.7)$$

Transforming back to the original coordinates, we have the solution to Eq. (2.3.1)

$$x = x_0 u_1\left(t + \frac{z_1}{2}\right) + x'_0 u_2\left(t + \frac{z_1}{2}\right) \quad . \quad (2.3.8)$$

Generally, $x'_0 \ll 1$, so from Eqs.(2.3.4), (2.3.5) and (2.3.8) we see that a particle at z_1 would be focused to the axis at time $t_0 \sim \sigma_z/D$, or

$$t \sim \frac{\sigma_z}{D} - \frac{z_1}{2} \quad . \quad (2.3.9)$$

The focal point is thus at

$$z_2 = -2t - z_1 \sim -\frac{2\sigma_z}{D} \quad . \quad (2.3.10)$$

This means particles at different longitudinal positions z_1 in one bunch would all be focused to the same point $z_2 \sim 2\sigma_z/D$, but at different times.

This naïve picture, however, contradicts simulation results. Two diagnoses were performed to monitor the detail processes of beam focusing in this regime. Figure 5 shows the time evolution of the average radius $\bar{r}(t, z)$ of a set of selected z -slices with z_1 ranging from $-2\sigma_z$ to $+2\sigma_z$ for $D = 1.0$ and $A = 0.05$. Here \bar{r} is defined as

$$\bar{r} \equiv \left\{ 2 \int_0^\infty [n_r(r)]^2 r dr \right\}^{-1/2}, \quad (2.3.11)$$

where the radial particle distribution function $n_r(r)$ is normalized such that $\int n_r(r) r dr = 1$. The above definition is equivalent to the definition of the standard deviation σ_0 in the limit of a Gaussian distribution, but in general it puts more weight on the radii that have higher particle densities. This is particularly inspired by the observation that during the collision a bunch tends to develop into a core and a halo, and the conventional definition of the *rms* value would not reflect the crucially important role of the core.

One finds in Fig. 5 that most particles at different z 's are focused almost simultaneously, at $t \sim 0.8 \sigma_z/c$, which differs with Eqs. (2.3.9) and (2.3.10). This fact is also reflected by the relatively short duration of the second peak in dH_D/dt . Indeed, the full-width half-maximum (FWHM) of the second peak turns out to be around $0.4 \sigma_z/c$ throughout the range of $0.7 \lesssim D \lesssim 3$. One further diagnosis is shown in Fig. 6 for dH_D/dz as a function of z . This is the cumulative contribution of each z -slice of one beam to the luminosity enhancement. If all the particles are focused at the same z_2 , as the strong-weak picture suggests, then dH_D/dz must show a sharp spike. On the contrary, Fig. 6 shows a smooth curve manifesting the longitudinal Gaussian distribution of the beam.

To account for these facts, we proceed by including the deformation of the on-coming beam to the first order in D . To this order, the deformation of a longitudinal slice at z_1 is given by Eq. (2.2.5), and that for the on-coming beam is obtained by simply replacing z_1 by $z_2 = -2t - z_1$, i.e.,

$$n_{r1}(r, t, z_2 = -2t - z_1) = n_{r0}(r) \left[1 + \frac{4Nr_e}{\gamma} \left(\frac{1}{n_{r0}} \frac{dn_{r0}}{dr} f_0 + n_{r0} \right) g(z_1) \right]. \quad (2.3.12)$$

It is interesting to observe that t does not appear on the R.H.S. of the above equation. We can thus improve the unperturbed equation of motion by replacing $f_0(r)$ with

$$f_1(r, z_1) = \frac{1}{r} \int_0^r n_{r1}(r, t, z_2 = -2t - z_1) r dr. \quad (2.3.13)$$

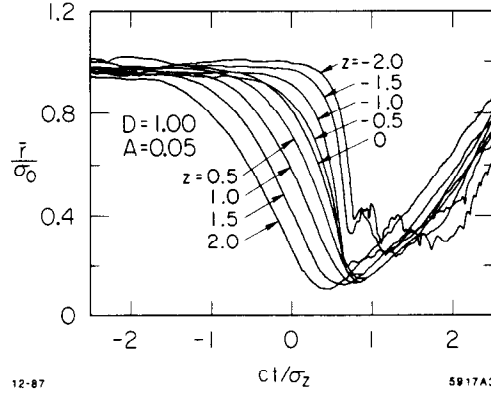


Fig. 5. Time evolution of the average radius \bar{r} (in units of σ_0) of a set of selected z -slices with z_1 ranging from $-2\sigma_z$ to $+2\sigma_z$ for $D = 1.0$ and $A = 0.05$. Notice that in this regime of D , different slices are focused to their minimum radius at about the same time, in this case at $t \sim 0.8\sigma_z/c$.

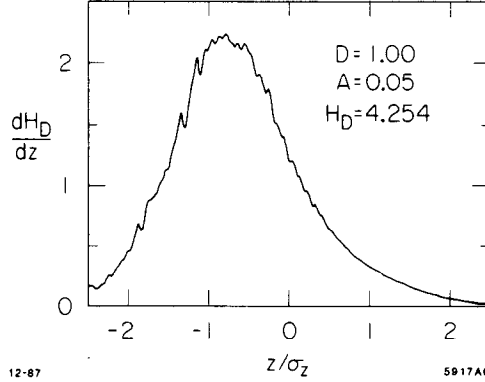


Fig. 6. Cumulative contribution of the luminosity enhancement factor dH_D/dz as a function of z . The Gaussian-like distribution indicates the simultaneity of the focusing process for different z -slices.

Substituting Eq. (2.3.12) into Eq. (2.3.13), we find a simple expression:

$$f_1(r, z_1) = f_0(r) \left[1 + \frac{4Nr_e}{\gamma} n_{r0}(r) g(z_1) \right]. \quad (2.3.14)$$

Actually, the above inclusion of the deformation of the on-coming beam, with the disruption parameter D intact, can also be interpreted as the inclusion of the modification of D to the next order, namely,

$$D \rightarrow D \left[1 + \frac{4Nr_e}{\gamma} n_{r0}(r) g(z_1) \right] . \quad (2.3.15)$$

with the distribution $f_0(r)$ unchanged. From this viewpoint the focusing force for the bunch core near the axis is increased by a factor:

$$1 + \frac{4Nr_e}{\gamma} n_{r0}(r) g(z_1) = 1 + 4D \frac{g(z_1)}{\sigma_z} . \quad (2.3.16)$$

Once this is seen, the result from the strong-weak picture (or the first order expansion in D) can be readily modified to include the next order in D . Namely, the focal point should occur at

$$t \sim \frac{\sigma_z}{D [1 + 4Dg(z_1)/\sigma_z]} - \frac{z_1}{2} . \quad (2.3.17)$$

From the definition of $g(z_1)$, we find for small z_1

$$4 \frac{g(z_1)}{\sigma_z} = \frac{1}{\sqrt{2\pi}} - \frac{1}{2} \frac{z_1}{\sigma_z} + \dots . \quad (2.3.18)$$

This implies that the z_1 dependence in Eq. (2.3.17) is almost cancelled provided that D is not too large (e.g., of order unity). Thus the minimum beam size occurs at the time

$$t \sim t_f(D) \equiv \frac{\sigma_z}{D (1 + D/\sqrt{2\pi})} . \quad (2.3.19)$$

We are now ready to derive the luminosity enhancement factor H_D . The beam size of the slice at z_1 can be derived from Eq. (2.3.8) as

$$\begin{aligned} \sigma_1^2 &= \langle x_0^2 \rangle u_1^2 \left(t + \frac{z_1}{2} \right) + \langle x_0'^2 \rangle u_2^2 \left(t + \frac{z_1}{2} \right) \\ &= \sigma_0^2 \left[u_1^2 \left(t + \frac{z_1}{2} \right) + \left(\frac{1}{\beta^*} \right)^2 u_2^2 \left(t + \frac{z_1}{2} \right) \right] . \end{aligned} \quad (2.3.20)$$

Considering that the primary contribution to H_D comes essentially from the high particle densities near the focii of both bunches, we concentrate on the beam size around $t \simeq t_f(D)$, where $u_1(t_f) = 0$. Thus Eq. (2.3.20) becomes

$$\sigma_1^2 \simeq \sigma_0^2 \left\{ \left[\dot{u}_1(t_f) \right]^2 (t - t_f)^2 + \left[\frac{u_2(t_f)}{\beta^*} \right]^2 \right\}$$

$$= \sigma_0^2 \left[\frac{9D}{16} \left(\frac{t-t_f}{\sigma_z} \right)^2 + \frac{16A^2}{9D} \right], \quad (2.3.21)$$

where Eqs. (2.3.4) and (2.3.5) have been used. The same expression holds for σ_2^2 of the second beam near $t \simeq t_f$. The enhancement factor is therefore

$$\begin{aligned} H_D &= \int dz_1 dz_2 \frac{1}{2\pi\sigma_z} \exp \left\{ -\frac{z_1^2 + z_2^2}{2\sigma_z^2} \right\} \left[\frac{2\sigma_0^2}{\sigma_1^2 + \sigma_2^2} \right] \\ &= 2 \int ds dt \frac{1}{2\pi\sigma_z} \exp \left\{ -\frac{s^2 + t^2}{\sigma_z^2} \right\} \left[\frac{9D}{16} \left(\frac{t-t_f}{\sigma_z} \right)^2 + \frac{16A^2}{9D} \right]^{-1} \\ &= \frac{1}{\sqrt{\pi}} \int \frac{dt}{\sigma_z} \exp \left\{ -\frac{t^2}{\sigma_z^2} \right\} \left[\frac{9D}{16} \left(\frac{t-t_f}{\sigma_z} \right)^2 + \frac{16A^2}{9D} \right]^{-1}. \end{aligned} \quad (2.3.22)$$

Since the contribution to H_D essentially comes from around $t \sim t_f$, we can approximately carry out the above integral as

$$H_D \simeq \frac{\sqrt{\pi}}{A} \exp \left\{ \frac{-1}{[D(1 + D/\sqrt{2\pi})]^2} \right\}. \quad (2.3.23)$$

Unfortunately, this expression does not fit the transition regime in Fig. 4 too well numerically. In particular, it is too sensitive to A , and Eq. (2.3.22) gives too sharp a peak in dH_D/dt . The disagreement mainly comes from the fact that t_f is not strictly z_1 independent. The residual z_1 dependence in Eq. (2.3.17) would break the simultaneity of focusing among all the z -slices. As a result, at time t_f when a slice at z_1 reaches its minimum size σ_1 , the overlapping oncoming slice at z_2 may not have reached its minimum yet. This slight mismatch between σ_1 and σ_2 would potentially relax the sensitivity of H_D on A , as in Eq. (2.3.23).

To incorporate the residual z_1 dependence in t_f , numerical integration will be needed. Our result here, however, does indeed qualitatively explain the essential physical process which dominates the transition regime: namely, the luminosity in the transition regime is contributed primarily from a very narrow window of collision time when the longitudinal slices from head to tail of each bunch are focused to their minimum size almost simultaneously.

2.4 Pinch Confinement of Bunch Core

In the large D regime ($D \gtrsim 5$) the most striking phenomena is the *confinement* of a large fraction of bunch particles near the axis within a small equilibrium radius throughout the course of collision. We call this portion of the bunch the *core*, as

opposed to the *halo* particles that come from either never being focused to the axis or being focused but escaping. The occurrence of this phenomena, however, is nothing like a phase transition that appears abruptly at a particular value of D . In fact, we already see certain signatures from the slices near the bunch tail in Fig. 5, where slices at $z = -1.0$, -1.5 and -2.0 tend to stay at a pinched radius. This is why we called the regime for medium D the *transition regime*.

In this section we devise an analytic description of the large D regime guided by simulation results. Since the luminosity essentially comes from the confined core, we will emphasize the behavior of the core. This is handled, again, by the mean radius \bar{r} of a longitudinal slice introduced in Eq. (2.3.11). However, for the sake of mathematical simplicity, the transverse distributions of each longitudinal slice is assumed to be Gaussian at any time. The evolution of the beam size is described by the *rms* beam size $\sigma_j(z_j, s)$ of a slice at z_j that comes to s . Since we assume equal beams, we have by mirror symmetry

$$\sigma_1(z, s) = \sigma_2(z, -s) \quad . \quad (2.4.1)$$

In the linear approximation of the focusing force, the equation of motion of a particle at z_1 in the first beam is given by

$$\frac{d^2 x}{ds^2} + K_1(z_1, s) x = 0 \quad , \quad (2.4.2)$$

with

$$K_1(z_1, s) = \frac{2Nr_e}{\gamma} \left\{ \frac{n_z(z_2)}{[\bar{\sigma}_2(z_2, s)]^2} \right\}_{z_2 = z_1 - 2s} \quad . \quad (2.4.3)$$

When D is very large, the actual beam size is rapidly oscillating during the collision. We may smooth out this fluctuation in the focusing force K_1 . In this sense we have introduced $\bar{\sigma}_2$ in Eq. (2.4.3), where the bar indicates a smoothing over some short interval of s . Our task is to solve Eq. (2.4.2) to obtain $x(z_1, s)$ and from which to deduce the beam size σ_1 so as to be self-consistent with $\bar{\sigma}_2$ in K_1 .

In the case where D is very large and the particle in consideration is well inside the oncoming bunch (i.e., $|z_2| \lesssim (\text{some factor}) \times \sigma_z$), the WKB approximation is suitable to solve Eq. (2.4.2). Thus, in this case we have

$$x(z_1, s) \simeq \frac{\sigma_0}{[\sigma_z^2 K_1(z_1, s)]^{1/4}} (C_1 \cos \theta_1 + C_2 \sin \theta_1) \quad , \quad (2.4.4)$$

where

$$\theta_1 = \int_{s_0}^s \sqrt{K_1(z_1, s)} ds \quad . \quad (2.4.5)$$

Here we have introduced dimensionless constants C_1 and C_2 . In order to express them in terms of the initial condition x_0 and x'_0 , we need a solution near the head of the oncoming bunch, where WKB fails. This will be discussed later.

Since $\cos \theta_1$ and $\sin \theta_1$ oscillate very rapidly, we may put $\overline{\cos^2 \theta_1} = \overline{\sin^2 \theta_1} = 1/2$ and $\overline{\cos \theta_1 \sin \theta_1} = 0$. Then, we have

$$\overline{x^2(z_1, s)} = \frac{\sigma_0^2}{\sigma_z \sqrt{K_1(z_1, s)}} \frac{1}{2} (C_1^2 + C_2^2) \quad (2.4.6)$$

To get the smoothed beam size we average Eq. (2.4.6) over the initial distribution, from which we get

$$\bar{\sigma}_1^2(z_1, s) = \langle \overline{x^2(z_1, s)} \rangle = \frac{C \sigma_0^2}{\sigma_z \sqrt{K_1(z_1, s)}} \quad (2.4.7)$$

with

$$C = \left\langle \frac{1}{2} (C_1^2 + C_2^2) \right\rangle, \quad (2.4.8)$$

where $\langle \rangle$ denotes the average over the initial distribution. Then, we get from Eqs. (2.4.3) and (2.4.7)

$$\bar{\sigma}_1^2(z_1, s) = \frac{C}{\sqrt{2D}} \left[\frac{\sigma_0 \bar{\sigma}_2(z_2, s)}{\sqrt{\sigma_z n_z(z_2)}} \right]_{z_2 = z_1 - 2s} \quad (2.4.9)$$

Similarly, for the second beam

$$\bar{\sigma}_2^2(z_2, s) = \frac{C}{\sqrt{2D}} \left[\frac{\sigma_0 \bar{\sigma}_1(z_1, s)}{\sqrt{\sigma_z n_z(z_1)}} \right]_{z_1 = z_2 + 2s} \quad (2.4.10)$$

Now we can solve Eqs. (2.4.9) and (2.4.10) self-consistently with the result

$$\bar{\sigma}_1(z_1, s) = \frac{C \sigma_0}{\sqrt{2D}} \left[\sigma_z n_z(z_1) \right]^{-1/6} \left[\sigma_z n_z(z_2) \right]^{-1/3} \Big|_{z_2 = z_1 - 2s} \quad (2.4.11)$$

Inserting into Eq. (2.4.3) we obtain

$$K_1(z_1, s) = \frac{4D^2}{C^2 \sigma_z^2} \left[\sigma_z n_z(z_1) \right]^{2/3} \left[\sigma_z n_z(z_2) \right]^{4/3} \Big|_{z_2 = z_1 - 2s} \quad (2.4.12)$$

Here we have a remarkable formula saying that the beam size is determined only by local variables; namely, the longitudinal density of the beam of interest at z_1

and the longitudinal density of the oncoming beam at the same position. All the history of the particle is packed in one single parameter C . Keep in mind, however, that Eqs. (2.4.11) and (2.4.12) do not apply to the head and the tail of the bunches.

Figure 7 shows the time evolution of the beam size for five z -slices at $z_1 = 1.0, 0.5, 0, -0.5$ and $-1.0 \sigma_z$ for $D = 100$ and $A = 0.05$. These five curves are then overplotted in Fig. 7(f). One finds that there is no distinctive difference among the five curves except for the shift in time according to their locations in the bunch. The slices abruptly shrink when entering the oncoming beam and soon reach some equilibrium "core" with small and rapid wiggles and a slow variation of the mean radii. The rapid wiggles are related to the oscillations of $\cos \theta_1$ and $\sin \theta_1$, whereas the slow variation agrees well with $[n_z(z_2)]^{-1/3} \propto \exp [(z_1 - 2s)^2 / 6\sigma_z^2]$ in Eq. (2.4.11), which ensures the validity of the WKB approximation.

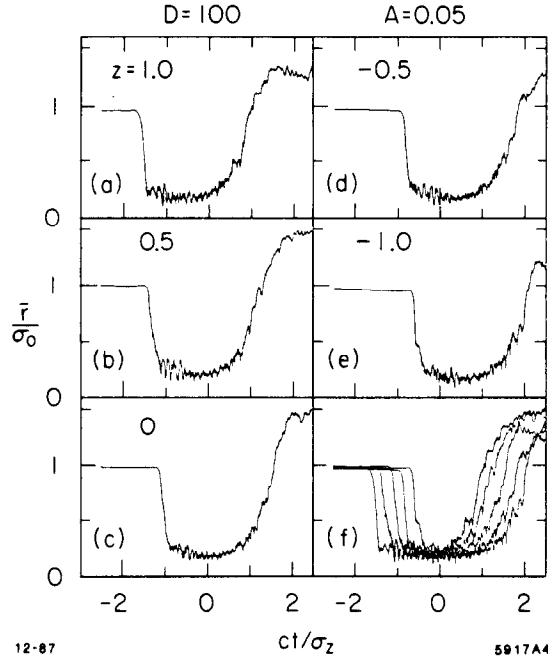


Fig. 7. Time evolution of the beam size for five selected z -slices at $z_1 = 1.0, 0.5, 0, -0.5$, and $-1.0\sigma_z$, for $D = 100$ and $A = 0.05$, shown in the figure from 7(a) to 7(e), respectively. The five figures are then overplotted in 7(f). A confined bunch core can be obviously seen.

In order to find H_D we have to express C_1 , C_2 and C in terms of the initial conditions. To this end we need a drastic approximation. The fact that the beam size suddenly reduces to a small value suggests that we may ignore the focusing

force before the particles are focused to the core. Therefore, we shall assume that the focusing force K_1 is given by Eq. (2.4.12) when z_2 is well inside the oncoming beam but is zero near the beginning and the end of the collision. The boundary is determined by the limit where WKB fails. The condition that the WKB is valid is given by

$$\left| \frac{d}{ds} \frac{1}{\sqrt{K_1}} \right| \lesssim 1 \quad (2.4.14)$$

Since z_1 is a constant for a given particle, we can rewrite Eq. (2.4.12) as

$$K_1 = \frac{k^2}{\sigma_z^2} \exp \left\{ -\frac{8s'^2}{3\sigma_z^2} \right\} \quad (2.4.15)$$

with

$$\begin{cases} s' = s - \frac{z_1}{2} \\ k = \sqrt{\frac{2}{\pi}} \frac{D}{C} \exp \left\{ -\frac{z_1^2}{6\sigma_z^2} \right\} \end{cases} \quad (2.4.16)$$

We shall ignore $\exp(-z_1^2/6\sigma_z^2)$, assuming that our particle is nowhere near the head and the tail of the beam. The solution of Eq. (2.4.14) for $s' < 0$ is

$$s' \gtrsim s'_0 \quad (2.4.17)$$

where $s'_0 (< 0)$ is a solution to

$$\frac{8(-s'_0)}{3 k \sigma_z} \exp \left\{ \frac{4s'^2_0}{3\sigma_z^2} \right\} = 1 \quad (2.4.18)$$

and is approximately given by

$$\frac{s'_0}{\sigma_z} \simeq - \sqrt{\frac{3}{8} \ell n \left(\sqrt{\frac{3}{8\pi}} \frac{D}{C} \right)} \quad (2.4.19)$$

The above s'_0 is thus the boundary that partitions the two zones for zero and finite K_1 's. Note that at $s' = s'_0$ K_1 is given by

$$K_1(s'_0) = \frac{9}{32\pi} \left(\frac{k}{\sigma_z C} \right)^2 \left(\frac{\sigma_z}{s'_0} \right)^2 \simeq \frac{3}{2\pi^2} \left(\frac{D}{\sigma_z C^2} \right)^2 \left[\ell n \left(\sqrt{\frac{3}{8\pi}} \frac{D}{C} \right) \right]^{-1} \quad (2.4.20)$$

The solution with the initial condition x_0 and x'_0 at $s' = s'_0$ is then

$$x = x_0 \left[\frac{K_1(s'_1)}{K_1(s')} \right]^{1/4} \cos \theta + x'_0 \left[\frac{1}{K_1(s'_0) K_1(s')} \right]^{1/4} \sin \theta \quad (2.4.21)$$

where

$$\theta = \int_{s'_0}^{s'_1} \sqrt{K_1(s')} ds' \quad (2.4.22)$$

Note that we have ignored the derivative of K_1 , which is always valid whenever the WKB approximation is applicable. Rigorously speaking, we should impose the initial condition at $s = 0$, not at $s'_1 = s'_0$. Our treatment is justified because for very small A the deflecting angle x'_0 at $s'_1 = s'_0$ is much smaller than σ_0 , which is the typical value of x_0 .

Comparing Eqs. (2.4.21) and (2.4.4) we have

$$\begin{cases} C_1 = [\sigma_z^2 K_1(s'_1)]^{1/4} \frac{x_0}{\sigma_0} = \left[\frac{2}{3} \left(\frac{\pi C^2}{D} \right)^2 \ell n \left(\sqrt{\frac{3}{8\pi}} \frac{D}{C} \right) \right]^{-1/4} \frac{x_0}{\sigma_0} \end{cases} \quad (2.4.23)$$

$$\begin{cases} C_2 = [\sigma_z K_1(s'_1)]^{-1/4} \frac{\sigma_z x'_0}{\sigma_0} \end{cases} \quad (2.4.24)$$

Averaging over the initial distribution gives

$$\langle C_1^2 \rangle = \frac{D}{\pi C^2} \left[\frac{2}{3} \ell n \left(\sqrt{\frac{3}{8\pi}} \frac{D}{C} \right) \right]^{-1/2} \quad (2.4.25)$$

and

$$\langle C_1^2 \rangle \langle C_2^2 \rangle = \frac{\langle x_0^2 \rangle}{\sigma_0^2} \frac{\sigma_z^2 \langle x_0'^2 \rangle}{\sigma_0^2} = A^2 \quad (2.4.26)$$

The latter merely insures the conservation of the linear emittance. Since we assume $A \ll 1$ and $D \gg 1$, we have $\langle C_1^2 \rangle \gg \langle C_2^2 \rangle$. Therefore,

$$C^2 = \frac{1}{2} \langle C_1^2 + C_2^2 \rangle \simeq \frac{1}{2} \langle C_1^2 \rangle \quad (2.4.27)$$

which, together with Eq. (2.4.25), determines C self-consistently. We now get

$$C = \left(\frac{D}{2\pi} \right)^{1/3} \left[\frac{2}{3} \ell n \left(\sqrt{\frac{3}{8\pi}} \frac{D}{C} \right) \right]^{-1/6} \quad (2.4.28)$$

While C still appears on the RHS of the expression, it varies only logarithmically. We may substitute C on RHS with some constant times $D^{1/3}$. As a good

approximation we get

$$C = \left(\frac{3D}{4\pi} \right)^{1/3} \left[\ln \left(\frac{D}{2} \right) \right]^{-1/6} \quad (2.4.29)$$

which agrees with the exact solution of Eq. (2.4.28) within 1% for $D \gtrsim 10$. Thus, the smoothed beam size in Eq. (2.4.11) is now written as

$$\bar{\sigma}_1(z_1, s) = \sigma_0 \left[\frac{9}{32\sqrt{2\pi}} \frac{1}{D \ln(D/2)} \right]^{1/6} \exp \left\{ \frac{z_1^2 + 2z_2^2}{12\sigma_z^2} \right\}_{z_2 = z_1 - 2s} \quad (2.4.30)$$

and the focusing function is

$$K_1(z_1, s) = \left[\frac{128}{9\pi} D^4 \ln \left(\frac{D}{2} \right) \right]^{1/3} \exp \left\{ \frac{z_1^2 + 2z_2^2}{3\sigma_z^2} \right\}_{z_2 = z_1 - 2s} \quad (2.4.31)$$

These formulas apply for

$$|z_2| \lesssim 2|s_0| \simeq \sqrt{\frac{3}{2} \ln \left(\frac{D}{2} \right)} \sigma_z \quad (2.4.32)$$

Let us now calculate the enhancement factor H_D . Analogous to Eq. (2.3.23) we have

$$H_D = \int dz_1 dz_2 \frac{\sigma_0^2}{\sigma_1^2(z_1, s) + \sigma_2^2(z_2, s)} \frac{1}{\pi \sigma_z^2} \exp \left\{ \frac{z_1^2 + z_2^2}{2\sigma_z^2} \right\}_{z_2 = z_1 - 2s} \quad (2.4.33)$$

Note that $2 ds dt = dz_1 dz_2$. If we replace σ_j in this expression with the smoothed radius $\bar{\sigma}_j$ in Eq. (2.4.29), we get

$$\bar{H}_D = 1.374 \left[D \ln \left(\frac{D}{2} \right) \right]^{1/3} \quad (2.4.34)$$

via numerical integration. As in the case of the transition regime where the slight mismatch between σ_1 and σ_2 should not be overlooked, in the confinement regime the rapid wiggling of the beam size also plays some role and, therefore, one needs to use σ_j instead of $\bar{\sigma}_j$. Averaging the square of Eq. (2.4.4) over the initial distribution and using Eqs. (2.4.25) and (2.4.30), we get

$$\begin{aligned} \sigma_1^2(z_1, s) &\equiv \langle x_1^2(z_1, s) \rangle \\ &= \sqrt{2\pi} \frac{\sigma_0^2}{D} \left(C^2 \cos^2 \theta_1 + \frac{A^2}{4} \sin^2 \theta_1 \right) \exp \left\{ \frac{z_1^2 + 2z_2^2}{6\sigma_z^2} \right\}_{z_2 = z_1 - 2s} \end{aligned} \quad (2.4.35)$$

At $\theta_1 = \pi/2$, we have the minimum beam size $\sigma_1 \simeq [(2\pi)^{1/4} A/2\sqrt{D}] \sigma_0$. Notice that if we ignore A^2 and replace $\cos^2 \theta_1$ by $1/2$, we recover the smoothed beam

size in Eq. (2.4.30). Nevertheless the finiteness of A can still contribute to the luminosity near the zeroes of $\cos \theta_1$. Substituting Eq. (2.4.35) into Eq. (2.4.33), the new H_D now reads

$$H_D = \frac{D}{\pi\sqrt{2\pi}} \int \frac{dz_1 dz_2}{\sigma_z^2} \exp \left\{ -\frac{3(z_1^2 + z_2^2)}{4\sigma_z^2} \right\} \\ \times \left[\exp \left\{ \frac{-z_1^2 + z_2^2}{12\sigma_z^2} \right\} \left(C^2 \cos^2 \theta_1 + \frac{A^2}{4} \sin^2 \theta_1 \right) \right. \\ \left. + \exp \left\{ \frac{z_1^2 - z_2^2}{12\sigma_z^2} \right\} \left(C^2 \cos^2 \theta_2 + \frac{A^2}{4} \sin^2 \theta_2 \right) \right]_{z_2 = z_1 - 2s}^{-1} \quad (2.4.36)$$

Since θ_1 and θ_2 are strong functions of z_1 and z_2 , and $C^2 \gg A^2/4$, we can approximately integrate the above expression to obtain

$$H_D = -\frac{2D}{\pi^2\sqrt{2\pi} C^2} \int \frac{dz_1 dz_2}{\sigma_z^2} \exp \left\{ -\frac{3(z_1^2 + z_2^2)}{4\sigma_z^2} \right\} \ln \left[\frac{A}{\sqrt{2} C} \cosh \left(\frac{z_1^2 - z_2^2}{12\sigma_z^2} \right) \right] \quad (2.4.37)$$

for $A \ll C$. By numerical integration and by invoking Eq. (2.4.29), we finally obtain

$$H_D = \lambda_1 \left[D \ln \left(\frac{D}{2} \right) \right]^{1/3} \left\{ \frac{1}{6} \ln \left[\frac{D^2}{\lambda_2 \ln(D/2)} \right] - \ln A \right\} \quad , \quad (2.4.38)$$

where $\lambda_1 = 0.880$ and $\lambda_2 = 2.28$. The agreement with the simulation is not excellent but the $\ln A$ dependence is correctly expressed. We can also obtain dH_D/dt , discussed in Section 2.1, by replacing $dz_1 dz_2$ in Eq. (2.4.37) with $2 ds dt$ and by integrating over s . Since only small $|z_1|$ and $|z_2|$ contribute in the integral, we may ignore the variation of \cosh in Eq. (6.37) as a rough approximation. In so doing, we obtain

$$\frac{dH_D}{dt} \simeq \frac{\sqrt{3}}{\sqrt{2\pi}\sigma_z} H_D \exp \left\{ -\frac{3t^2}{2\sigma_z^2} \right\} \quad (2.4.39)$$

Comparing this expression with the unperturbed dH_0/dt of Eq. (2.1.5), one finds that dH_D/dt for large D is indeed Gaussian with a slightly larger coefficient for t^2 in the exponent. This fact agrees with the simulation results quite well. (Compare the figure for $D = 100$ versus that for $D = 0.2$ in Fig. 4.) Notice that the functional behavior $\exp(-3t^2/2\sigma_z^2)$ comes solely from the WKB part. On the other hand, the overall factor in Eq. (2.4.39), which comes from the truncation of K_1 at the head of the bunch, like the case for H_D , does not numerically reproduce the simulation results.

2.5 Luminosity Enhancement With Offset

Since the asymmetry in distributions tends to shift the center-of-gravity of the beams, it gives rise to the same effect as the initial alignment offsets. For this reason our study on the effect of imperfections is concentrated on initial offsets only.

As will be discussed in the next section, an initial offset triggers a kink instability, especially when the disruption parameter becomes large. As it occurs, this instability is not always harmful because, in the initial phase of the instability, the beams always tend to find each other, which prevents the otherwise rapid degradation of the luminosity for large initial offsets. Figure 3 shows the luminosity enhancement factor as a function of offset Δ_y (in units of σ_y) for various values of D_y . The dotted curve is the geometrical enhancement factor without beam-beam force, which is equal to $\exp(-\Delta_y^2/4)$. UGG distribution is used and $A_y = 0.2$ for all curves. The up-down symmetry is not enforced except for the cases at $\Delta_y = 0$.

From Fig. 8 one finds that the tolerance on alignment offset reaches an optimum for values of D_y between 5 and 10. Within this range of D_y , H_D is still above unity even at $\Delta_y \sim 3$. Beyond this region of D_y the beam-breakup becomes severe, while below the beam-beam attraction is not yet strong enough.

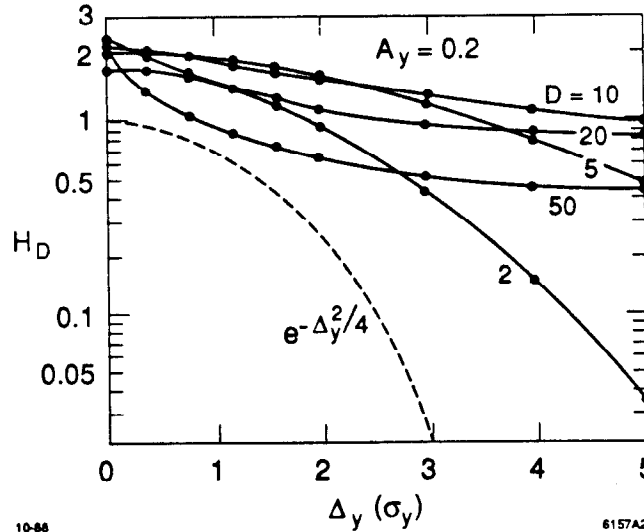


Fig. 8. H_D as a function of offset Δ_y for flat beams.

The same data as in Fig. 8 is replotted in Fig. 9 as a function of D_y , and each curve corresponds to a fixed value of Δ_y . (The region of large D_y and small Δ_y is not very accurate because of its sensitivity to computing errors.) One sees a saturation and decrease of H_D as a function of D_y unless $\Delta_y = 0$. One also

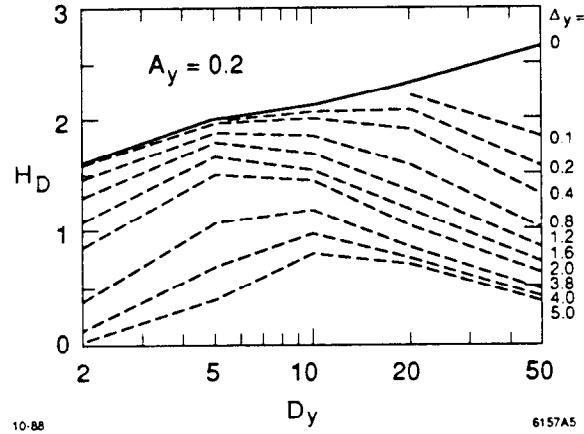


Fig. 9. H_D as a function of D_y for flat beams.

notices that the curves with small offsets, e.g., $\Delta_y = 0.2$, resemble the results in Refs. 5 and 6, except that our offset was explicitly introduced. In designing a linear collider, one needs to estimate H_D for the chosen D and A . This depends on the assesment of potential imperfections of beam-beam collision. Though arbitrary, it may be safer to adopt the curve for $\Delta_y = 0.2$ or 0.4 , instead of $\Delta_y = 0$, as the effective enhancement factor.

Similar exercise for round beams are shown in Fig. 10 for D up to 50. Here we find the same generic behavior as in the case for flat beams.

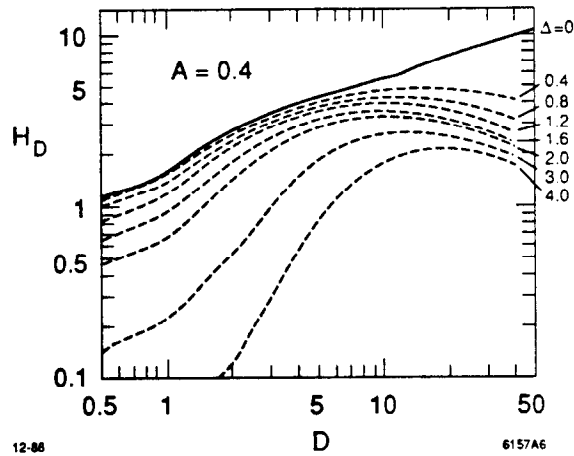


Fig. 10. H_D as a function of offset Δ for round beams.

2.6 Disruption Angles

One important piece of information for linear collider design is the expected disruption angle. Knowledge of the maximum disruption angle is essential to determine the aperture of the last element in a final focusing system, so as to avoid being showered by the debris from the beam-beam collision.

For round beams, the simulation results of the maximum and the *rms* disruption angle reduction factors, H_{θ}^{max} and H_{θ}^{rms} , are plotted in Figs. 11 and 12, respectively. The curves for $A = 0$ in the two figures reasonably agree with the previous results.⁵ These curves for zero emittance can be well-explained theoretically,⁶ which predicts the following generic functional behavior for both $H_{\theta,0}^{max}$ and $H_{\theta,0}^{rms}$ for $A = 0$, i.e., a linear increase for $D \ll 1$ and a $1/\sqrt{D}$ suppression for $D \gg 1$:

$$H_{\theta,0} \sim \begin{cases} a + bD, & D \ll 1, \\ \frac{c}{\sqrt{D}}, & D \gg 1, \end{cases} \quad (2.6.1)$$

where a , b and c are some numerical coefficients which are different for maximum and *rms* angles, and which are to be fixed by the simulations. From Figs. 11 and 12 we find

$$H_{\theta,0}^{max} \simeq \begin{cases} 0.87 + 1.57 D, & D \ll 1, \\ \frac{1.84}{\sqrt{D}}, & D \gg 1, \end{cases} \quad (2.6.2)$$

and

$$H_{\theta,0}^{rms} \simeq \begin{cases} 0.78 + 0.20 D, & D \ll 1, \\ \frac{0.67}{\sqrt{D}}, & D \gg 1. \end{cases} \quad (2.6.3)$$

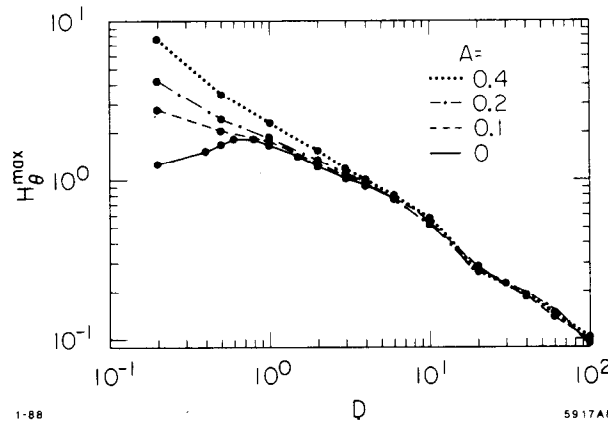


Fig. 11. Maximum disruption angle as a function D for round beams, computed with four different values of A .

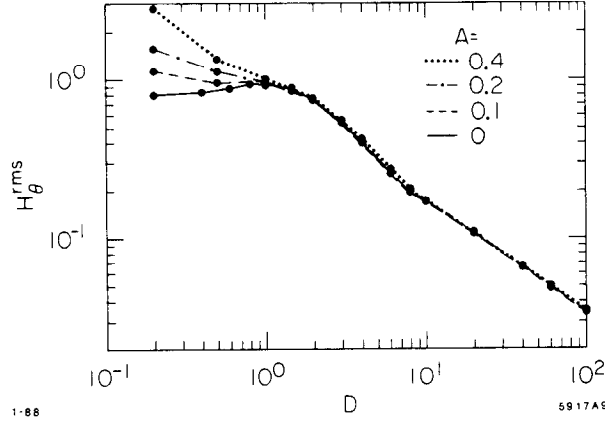


Fig. 12. Rms disruption angle as a function of D for round beams.

When $A \neq 0$, the inherent divergence of the beam cannot be overlooked when the disruption is small. The natural rms divergence angle of a beam is

$$\sigma'_{x,y} = \frac{\sigma_{x,y}}{\beta^*} = \frac{\sigma_0}{\beta^*}, \quad (2.6.4)$$

while

$$\sigma'_0 = \sqrt{\sigma'^2_x + \sigma'^2_y} = \sqrt{2} \sigma'_x. \quad (2.6.5)$$

Dividing both sides by θ_0 , as defined in Eq. (2.14), we have the contribution from finite emittance:

$$H_{\theta,\epsilon}^{rms} \equiv \frac{\sigma'_0}{\theta_0} = \sqrt{2} \frac{A}{D}, \quad (2.6.6)$$

where the definitions of A and D are used. The general expression for H_{θ}^{rms} is therefore

$$H_{\theta}^{rms} = \sqrt{(H_{\theta,0}^{rms})^2 + (H_{\theta,\epsilon}^{rms})^2}. \quad (2.6.7)$$

Inserting Eq. (2.6.3) for $H_{\theta,0}^{rms}$ and Eq. (2.6.6) for $H_{\theta,\epsilon}^{rms}$, the above expression fits all the curves in Fig. 11 very well. Notice that the contribution of the second term rapidly diminishes for D beyond unity. Thus the rms disruption angle is asymptotically independent of A .

The situation for the maximum disruption angle is slightly more complicated since the maximum natural divergence angle for Gaussian distributions is not well-defined. However, as is the case for $H_{\theta,0}$, the functional behavior of $H_{\theta,\epsilon}^{max}$ should be similar to that of $H_{\theta,\epsilon}^{rms}$, and the overall H_{θ}^{max} should be analogous to H_{θ}^{rms} in Eq. (2.6.7). This is evidenced by the similarity between Figs. 11 and 12, aside from the numerical differences.

Now we examine the flat beam deflections. If the disruption parameter is very small, the transverse location of a particle during collision is nearly constant. Then one can estimate the disruption angles θ_x and θ_y as functions of the initial transverse coordinates x_0 and y_0 . For very flat Gaussian beams we have

$$\theta_x = -\sqrt{\frac{\pi}{2}} D_x \frac{\sigma_x}{\sigma_z} \text{Im} \left[\frac{i}{\pi} \int_{-\infty}^{+\infty} \frac{\exp\{-t^2\} dt}{(x_0/\sqrt{2}\sigma_x) - t - i0} \right] , \quad (2.6.8)$$

$$\theta_y = -\sqrt{\frac{\pi}{2}} D_y \frac{\sigma_y}{\sigma_z} \left[\frac{2}{\sqrt{\pi}} \int_0^{y_0/\sqrt{2}\sigma_y} e^{-t^2} dt \right] e^{-x_0^2/2\sigma_x^2} . \quad (2.6.9)$$

where the quantities in the square brackets can be expressed by the complex error function $w(x_0/\sqrt{2}\sigma_x)$ and the real error function $\text{erf}(y_0/\sqrt{2}\sigma_y)$. Here the emittance is ignored. One finds that the maximum and *r.m.s.* disruption angle reduction factor to be

$$H_{\theta_{x,0}}^{rms} = 0.765 , \quad (x_0 = 1.31\sigma_x) \quad (2.6.10)$$

$$H_{\theta_{y,0}}^{rms} = \sqrt{\pi/2} , \quad (x_0 = 0, y_0 = \infty) \quad (2.6.11)$$

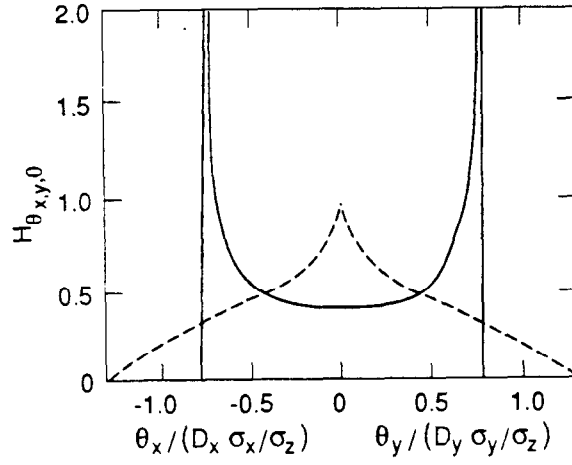
$$H_{\theta_{x,0}}^{rms} = \sqrt{\pi/(6\sqrt{3})} , \quad (2.6.12)$$

$$H_{\theta_{y,0}}^{rms} = \sqrt{\pi/(6\sqrt{3})} , \quad (2.6.13)$$

where the nominal angles $\theta_{x,0} = D_x \sigma_x / \sigma_z$ and $\theta_y = D_y \sigma_y / \sigma_z$ are assumed. These resemble the leading constant terms in Eqs. (2.6.2) and (2.6.3) when $D \ll 1$. (Rigorously speaking, for flat beams with large but finite aspect ratio, θ_y reaches a maximum near $y_0 \sim \sigma_x$ and then decreases; but this is not important.)

The distribution functions of $H_{\theta_{x,0}}$ and $H_{\theta_{y,0}}$ are shown in Fig. 13. The actual singularities at $\theta_x = \theta_{x,max}$ and $\theta_y = 0$ are not supposed to be as sharp as those in Fig. 13 because of finite emittance, various errors, and the disruption effect. However, we found from simulations that the qualitative difference between the horizontal and vertical angles still holds even for $D_{x,y}$ not much less than unity.

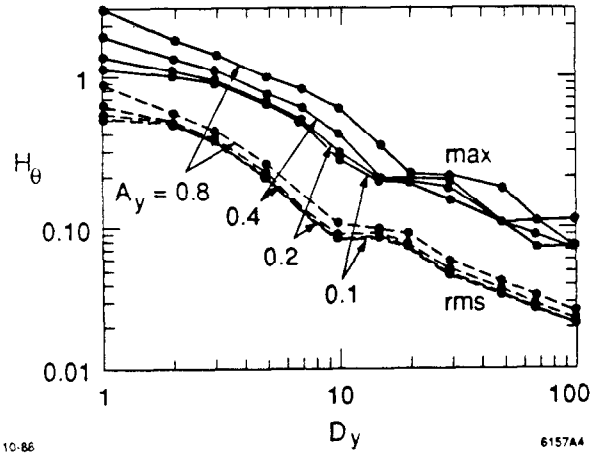
Figure 14 shows the maximum and *r.m.s.* vertical disruption angle reduction factor H_{θ_y} (θ_y in units of $D_y \sigma_y / \sigma_z$), as a function of D_y . Here we consider the case for small D_x only. As in the case for round beams, the dependence on A_y is not as significant as in the case of H_D except for the small D_y region, where the beam divergence is emittance dominated. (The distribution of initial σ_x is truncated at 2.5 standard deviations in the simulation.)



10-88

6157A7

Fig. 13. Distribution of $H_{\theta_{x,y},0}$ for small $D_{x,y}$.



10-86

6157A4

Fig. 14. Maximum and r.m.s. vertical disruption angle reduction factor. The four curves correspond to $A_y = 0.1, 0.2, 0.4, 0.8$, respectively.

The simulation results can roughly be fitted by

$$H_{\theta_y}^{rms} \sim \sqrt{\frac{\pi}{6\sqrt{3}}} \frac{1}{[1 + (0.5D_y)^5]^{1/6}} \quad (2.6.14)$$

and $H_{\theta_y}^{max} \sim 2.5H_{\theta_y}^{rms}$. Here the contribution of the initial emittance ($= A_y \sigma_y / \sigma_z$ for $\theta_{y,rms}$) has not been included. The reason that the angle does not increase linearly in D_y is that the particle trajectories are bent backwards and oscillate when D_y is large.

So far, the collision is assumed to be head-on. For flat beams the disruption angle in the presence of vertical offset is also important in determining the aperture of the final quads. The mean deflection angle of the entire bunch can be written in the form⁷⁾

$$\Theta_y = \frac{1}{2} \frac{\sigma_y}{\sigma_z} D_y H_c(D_y, \Delta_y) \quad , \quad (2.6.15)$$

where Δ_y is the vertical offset in units of σ_y and the weak dependence on A_y is ignored. For small disruptions, the function H_c approaches the following analytic form

$$H_c(D_y, \Delta_y) = \int_0^{\Delta_y} e^{-y^2/4} dy \quad . \quad (2.6.16)$$

Figure 15 shows H_c as a function of Δ_y computed by simulations, where UGG distribution is assumed.

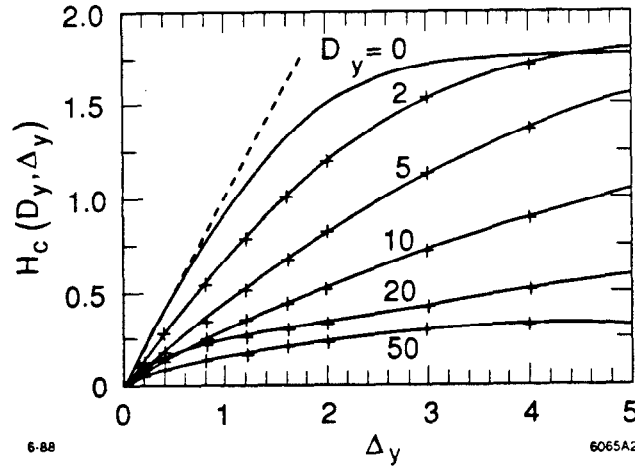


Fig. 15. Effective center-of-mass deflection. The curve for $\Delta_y = 0$ is analytic, while the rest are from simulation. The dashed line corresponds to the slope at the zero D_y and zero Δ_y limit, which is equal to $1/2$.

Roughly speaking, the maximum disruption angle in the presence of offsets is the sum of the center-of-mass deflection angle Θ_y and the maximum angle in the absence of offsets, $\theta_{y,max}$.

2.7 Kink Instability

If one of the beams is displaced vertically for some reason, this offset triggers a vertical oscillation and, when D is large, the oscillation is enhanced by the beam-beam force. This phenomena is known as the *kink instability*. Figure 16 shows a specific example.

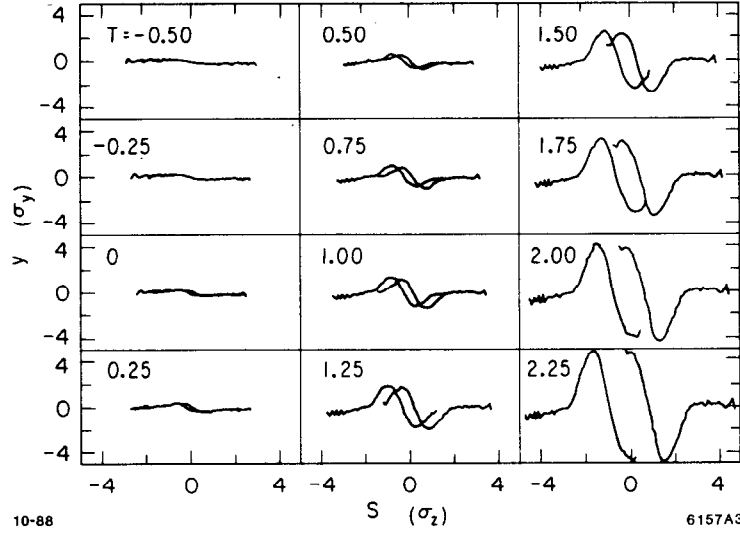


Fig. 16. An example of kink instability for $D = 20$, $A = 0.2$, and $\Delta_y = 0.2$

In the above figure the bunch is sliced longitudinally and the vertical coordinate y of the center-of-mass of each slice (in units of σ_y) is plotted against the longitudinal coordinate s (in units of σ_z). Each graph corresponds to a snapshot of the beam vertical position at a particular time t (in units of σ_z/c). The development of the instability can be seen in time sequence. The initial offset in this example is chosen to be $0.2\sigma_y$ (full) and the disruption parameter is $D_y = 20$.

For uniform beams and small amplitude oscillations, the equation of motion for the beam particles can be obtained from fluid dynamics (the flat beam version of the equation is given in Ref. 8),

$$\left[\frac{\partial}{\partial t} \pm \frac{\partial}{\partial s} \right]^2 y_{\pm} = -\omega_0^2 (y_{\pm} - y_{\mp}), \quad \omega_0^2 = \frac{\sqrt{2\pi} D_y}{6 \sigma_z^2} \quad (2.7.1)$$

where y_{\pm} is the y coordinate of e^+ and e^- beams. Consider the space-time variation of y_{\pm} to be of form $\exp\{ikz - i\omega t + \phi\}$. The non-trivial solution of the above equation should satisfy the following dispersion relation:

$$1 = \frac{\omega_0^2}{(\omega + k)^2} + \frac{\omega_0^2}{(\omega - k)^2} \quad (2.7.2)$$

The most unstable solution is found to be

$$y_{\pm} = \text{const.} \times \exp \left[\pm i \left(\frac{\sqrt{3}}{2} \omega_0 s - \frac{\pi}{6} \right) + \frac{1}{2} \omega_0 t \right] \quad (2.7.3)$$

This solution is in reasonable agreement with the simulation shown in Fig. 16. Namely, the phase difference between e^- and e^+ beams is varied to be $\pi/3$, and

the growth rate is as predicted. Furthermore, Fig. 16 clearly demonstrates the standing-wave nature of the kink instability, which agrees with the description of Eq. (2.7.3).

So far our discussion on the kink instability deals with collisions of two bunches. Another type of kink instability occurs during the collision of two bunch trains, each consists of N_B bunches. One of the major problems of such a multi-bunch operation is the interaction between bunches before and after their collisions at the central collision point. The i^{th} bunch in the electron bunch train will collide not only with the i^{th} bunch in the positron train, but also with the $j(< i)^{th}$ positron bunch before coming to the central collision point. Colliding two flat beams at a relatively large crossing angle can help to avoid unwanted direct encounters between the outgoing bunch debris and the incoming fresh bunches. However, due to the long range nature of the Coulomb interaction, there still exists undesirable interference between two separated bunches at a distance. Since the crossing angle cannot be made arbitrarily large due to the luminosity consideration, this long range interaction cannot be entirely suppressed. In fact, it imposes a severe restriction on the stability of the beams.

Consider the encounter between the n^{th} positron bunch after collision and the m^{th} ($m > n$) electron bunch before collision at a distance L from the collision point. A schematic diagram of the system is shown in Fig. 17. We assume that all the bunch encounters occur within the drift space around the central collision point.

According to Eq. (2.6.15), the center-of-mass deflection angle for the n^{th} positron bunch is

$$\Theta_{yn} = \frac{1}{2} \frac{\sigma_y}{\sigma_z} D_y H_c(D_y, \Delta_{yn}) \quad , \quad (2.7.4)$$

where Δ_{yn} is the relative offset between the m^{th} electron and the n^{th} positron bunch, in units of σ_y , at their closest encounter. The cumulative offset for the m^{th} bunch before arriving at the central collision point is therefore

$$\Delta_m = C \sum_{n < m} H_c(D_y, \Delta_n) + \delta_m \quad , \quad (2.7.5)$$

where δ_m is the initial offset of the m^{th} beam, and the coefficient C is

$$C = D_x D_y \left(\frac{\theta_d}{\theta_c} \right)^2 \quad , \quad (2.7.6)$$

and $\theta_d = \sigma_x / \sigma_z$ is the diagonal angle of the bunch.

The cumulative offset Δ_m (in units of $\delta(1 + C)^{m-1}$) is plotted as a function of the number of bunches in Fig. 18. Since the factor θ_d / θ_c must be larger than

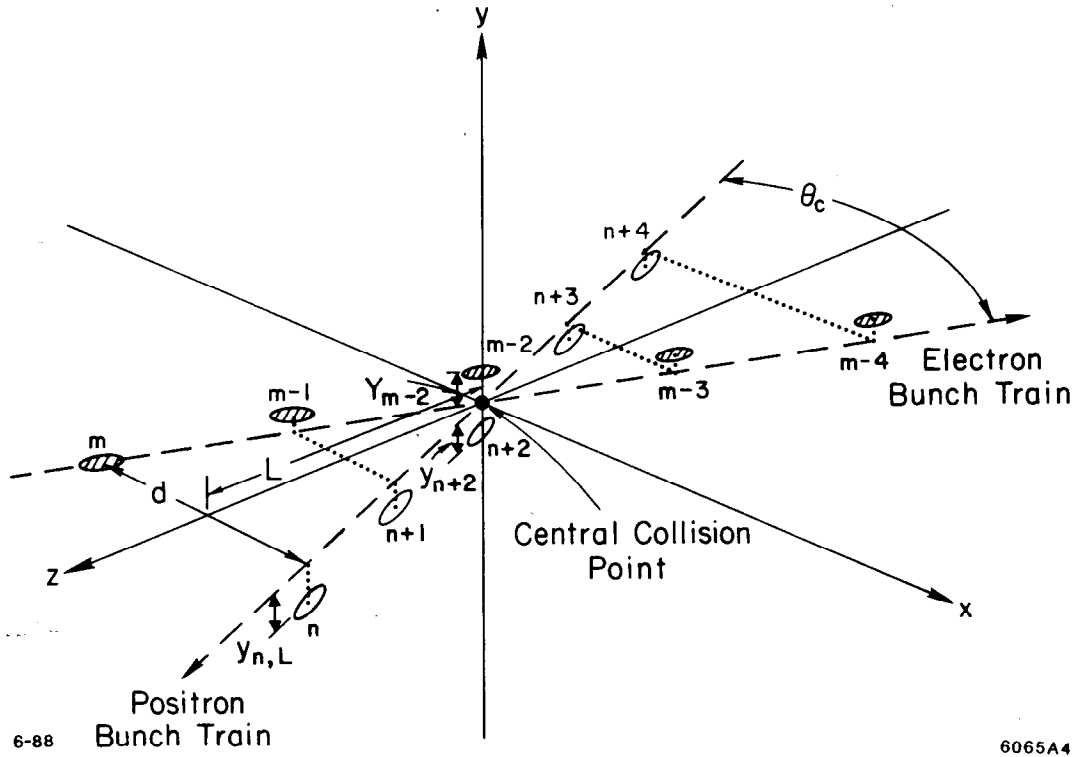


Fig. 17. A schematic diagram of multi-bunch collision.

unity in order that the crossing angle does not reduce the luminosity significantly. the condition for negligible growth of the instability, i.e., $\Delta_{yn} \lesssim \delta$, according to Fig. 17, is roughly

$$(N_B - 1) D_x D_y \lesssim 2 \quad . \quad (2.7.7)$$

This imposes a constraint on the allowable number of bunches per train.

3. BEAMSTRAHLUNG EFFECTS

The energy spectrum of the electrons is important for two reasons: (1) the *tip* of the spectrum, i.e., the distribution near the initial beam energy, provides information on the energy resolution for high energy physics events, and (2) the *tail* of the spectrum, i.e., the distribution of the low energy electrons, which had suffered severe energy loss through hard beamstrahlung, reveals the likelihood of finding large disruption angles. This second issue will be addressed in the next section.

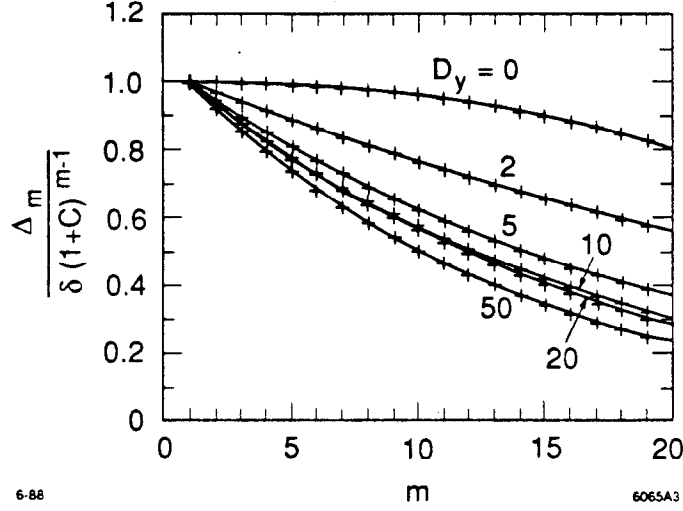


Fig. 18. Cumulative offset as a function of the number of bunches.

The energy spectrum of radiation can be characterized by the beamstrahlung parameter Υ , defined as

$$\Upsilon = \gamma \frac{B}{B_c} \quad , \quad (3.1)$$

where B is the effective field strength of the beam, and $B_c = m^2 c^3 / e \hbar \sim 4.4 \times 10^{13}$ Gauss is the Schwinger critical field. For historical reasons, this parameter is related to the parameter ξ introduced by Sokolov and Ternov, by a simple factor $3/2$:

$$\xi = \frac{(\text{critical energy})}{(\text{initial energy})} = \frac{3 r_e \gamma^2}{2 \alpha \rho} = \frac{3}{2} \Upsilon \quad , \quad (3.2)$$

where ρ is the instantaneous radius of curvature. Since the two parameters are trivially related, we shall employ either of them depending on the convenience of the situation. The typical value of ξ during collision is

$$\xi_1 = \frac{r_e^2 \gamma N}{\alpha \sigma_z \sigma_y} \frac{2}{1 + R} \quad , \quad (3.3)$$

where $R = \sigma_x / \sigma_y$ is the aspect ratio of the beam. The average value of ξ is a bit smaller than Eq. (3.3) (by about a factor $2/3$) but we adopt it for the better description of the spectrum tail which is contributed more effectively from beamstrahlung with larger ξ .

3.1 Energy Spectrum of Final Electrons

Let $\psi(E, t)$ be the energy spectrum function of electrons at time t normalized as $\int \psi(E, t) dE = 1$. We assume that the emission of a photon takes place in

infinitesimally short time instance, at least for linear colliders in the near future. Then the evolution of the spectrum function can be described by the rate equation

$$\frac{\partial \psi}{\partial t} = -N_\gamma(E)\psi(E, t) + \int_E^\infty F(E, E_1)\psi(E_1, t)dE_1 \quad (3.1.1)$$

Here, $N_\gamma(E)$ is the average number of photons per unit time and F is the radiation spectrum function; i.e., $F(E_2, E_1)dE_2$ is the transition probability of an electron from energy E_1 to the energy interval $(E_2, E_2 + dE_2)$ during time interval dt . Obviously, $F(E_2, E_1) = 0$ if $E_2 \geq E_1$ and F does not include the probability to stay at the same energy without photon emission. The sum over the whole energy range gives the number of photons:

$$\int_0^{E_1} F(E_2, E_1)dE_2 = N_\gamma(E_1) \quad (3.1.2)$$

The quantum-theoretical spectrum function F is well-known,

$$F(E', E) = \frac{N_{cl}}{\xi E'} f(\xi, y) \quad (3.1.3)$$

$$f(\xi, y) = \frac{3}{5\pi} \frac{1}{1 + \xi y} \left[\int_y^\infty K_{5/3}(x)dx + \frac{\xi}{1 + \xi y} \frac{2y}{\xi} K_{2/3}(y) \right]$$

with

$$y = \frac{\omega}{\omega_c} \frac{1}{1 - \omega/E} = \frac{1}{\xi} \frac{E - E'}{E'} = \frac{1}{\xi} \left(\frac{1}{\varepsilon} - 1 \right) \quad (3.1.4)$$

where K 's are the modified Bessel functions, N_{cl} the number of photons per unit time by the classical formula, ω the photon energy, and $\varepsilon = E'/E$ the fractional energy. The number of emitted photons per electron can be expressed as

$$N_\gamma = N_{cl} U_0(\xi), \text{ with } N_{cl} = 2.12 \frac{\alpha r_e N}{\sigma_x + \sigma_y} \quad (3.1.5)$$

where $U_0(\xi)$ is the ratio of the quantum-theoretical number of photons to that from the classical theory, and is found to be⁹⁾

$$U_0(\xi) = \frac{1 - 0.598\xi + 1.061\xi^{5/3}}{1 + 0.922\xi^2} \quad (3.1.6)$$

where the relative error is within 0.7%.

An approximate formula for the energy spectrum of electrons after collision can be therefore derived. The details are given in Ref. 10, where the spectral function $\psi(\varepsilon)$ ($\varepsilon = E/E_0$) is found to be

$$\psi(\varepsilon) \simeq e^{-N_\gamma} \left[\delta(\varepsilon - 1) + \frac{e^{-y}}{1 - \varepsilon} h(N_1 y^{1/3}) \right] , \quad (3.1.7)$$

with

$$\begin{aligned} h(x) &= \frac{1}{2\pi i} \int_{\lambda-i\infty}^{\lambda+i\infty} \exp(xp^{-1/3} + p) dp \quad (\lambda > 0) \\ &= \sum_{n=1}^{\infty} \frac{x^n}{n! \Gamma(n/3)} , \end{aligned} \quad (3.1.8)$$

and

$$N_1 = \frac{1}{1 + \xi_1 y} N_{cl} + \frac{\xi_1 y}{1 + \xi_1 y} N_\gamma . \quad (3.1.9)$$

(This formula does not exactly satisfy the normalization condition except for $\xi_1 \rightarrow 0$ which leads to $N_1 = N_\gamma = N_{cl}$.) The function $h(x)$ can be estimated very accurately by with relative error less than 2%. Figure 19 compares Eq. (3.1.7) with the simulation results using the parameters for the TLC and the ILC.¹¹⁾ The design parameters of the two colliders are summarized in Table 1. The histograms in Fig. 19 are from simulations and the dotted data are computed from Eq. (3.1.7). The agreement is excellent.

3.2 Maximum Deflection Angle

The particle which once lost a large fraction of its initial energy through beamstrahlung would, in principle, be severely deflected by the beam-beam field and cause background problems for high-energy experiments. Consider an electron which emits a hard photon at a particular time during the collision and results in an energy εE_0 , with $\varepsilon \ll 1$. The effective disruption parameter for this particle becomes D_x/ε and D_y/ε . One might think that Eqs. (2.6.10) and (2.6.11) are still applicable by replacing D by D/ε . However, the collision of a single particle on a beam with the disruption parameter D/ε is different from the collision between two beams with D/ε , although the qualitative feature is the same; i.e., the disruption angle increases linearly in D for $D \lesssim 1$ and more slowly for $D \gtrsim 1$.

A simulation was done by monitoring low-energy test particles through the collision process. The maximum deflection angle for a given ε is found to be roughly:

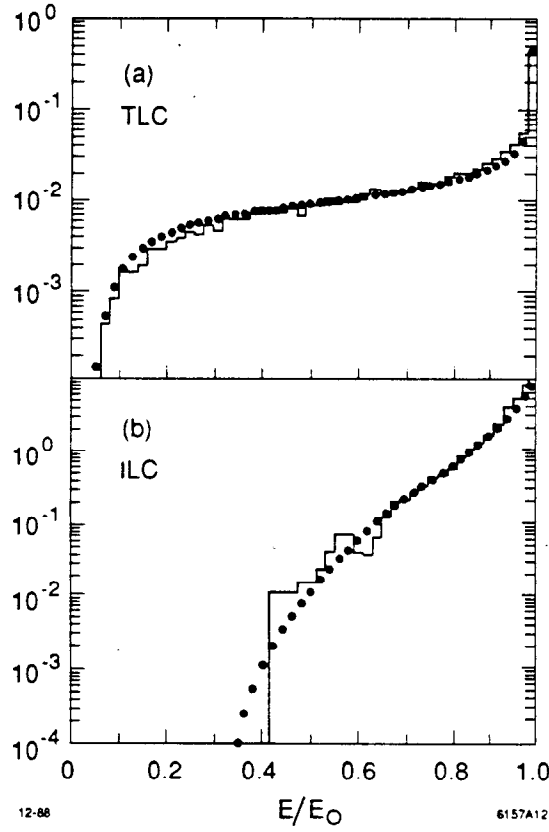


Fig. 19. Electron energy spectrum for TLC and ILC parameters.

$$\theta_{max} \sim \frac{\sigma}{\sigma_z} \frac{D/\epsilon}{\sqrt{1 + (0.75D/\epsilon)^{4/3}}} \quad , \quad (\epsilon \ll 1) \quad (3.2.1)$$

where $D = D_x(D_y)$ and $\sigma = \sigma_x(\sigma_y)$ for the horizontal (vertical) angle.

The minimum value of ϵ can, in principle, be as small as $1/\gamma$. But the real problem is about how small a ϵ should one care. Since the number of photons N_γ per beam particle for linear colliders in the near future is of order unity, the spectral function $\psi(\epsilon)$ given in Eq. (3.1.6) is always dominated by the factor e^{-y} in the spectrum tail, where $y \gg 1$ (in logarithmic sense). Therefore, if the acceptable background count is n out of N electrons, then the minimum ϵ of concern is approximately determined by $y = \log(N/n)$, or

$$\epsilon_{min} = \frac{1}{1 + \xi_1 \log(N/n)} \quad (3.2.2)$$

With this value of ϵ , one can directly estimate the maximum deflection angle using Eq. (3.2.1). Since the dependence on n is only logarithmic, one can set $n = 1$.

Table 1. Parameters for TLC and ILC ($\lambda_{rf} = 17$ mm)

	TLC	ILC
E_0 [TeV]	0.5	0.25
N	8×10^9	7×10^9
σ_x [nm]	190	440
σ_y [nm]	1	3
σ_z [μm]	26	65
R	190	147
ϵ_x [mrad]	2.58×10^{-12}	5.2×10^{-12}
ϵ_y [mrad]	2.33×10^{-14}	5.2×10^{-14}
D_x	0.033	0.027
D_y	6.27	3.9
A_x	0.0002	0.0017
A_y	0.60	0.37
* $\mathcal{L}/\mathcal{L}_0$	1.61	1.71
* δ	0.15	0.01
* N_γ	1.33	0.38
ξ_1	3.43	0.19

* Quantities computed by simulations.

Thus, for example, $\epsilon_{min} = 0.013$ (0.188), $\theta_{x,max} = 10$ (0.95) mrad and $\theta_{y,max} = 0.4$ (0.15) mrad for TLC (ILC) parameters.

4. ELECTRON-POSITRON PAIR CREATION

During the collision of the e^+e^- beams, there are finite probabilities that a photon will turn itself into a e^+e^- pair. Once the e^-e^+ pairs are created with lower energies in general, one of the two particles in each pair will have the same sign of charge as the oncoming beam. (For the sake of argument, consider a low energy e^+ moving against the positron beam). Unlike the case of a low-energy e^- moving against a positron beam, where the potential tends to confine the particle in the beam profile, in the case of a positron the potential is unconfining and the particle can, in principle, be deflected by a large angle and thus create

severe background problems. This effect would therefore impose a constraint on the final focus design.

It occurs that the e^+e^- pair can be created by either real or virtual photons. These photons, in turn, can pair-produce through two different physical processes, namely, the *coherent* and the *incoherent* processes. While the incoherent process has been studied earlier,^{13,14)} it is recently realized¹²⁾ that the coherent process is even more severe.

Recall that in the case of radiation by $e^-(e^+)$ during beam-beam collision, there are essentially two mechanisms that induce the radiation. Namely, there is an "incoherent" process, or Bremsstrahlung, associated with the individual e^-e^+ scatterings, and there is also a "coherent" process due to the interaction between the radiating charged particle and the macroscopic beam-beam EM field. At high energies and strong fields, the coherent process tends to dominate over the incoherent one. This is actually why our discussion on beam energy loss has been focused only on the beamstrahlung process.

The beamstrahlung photons once emitted would have to travel through the remainder of the oncoming beam before entering into free space, and would therefore turn themselves into e^-e^+ pairs. Analogous to the case of radiation, photon pair creation also involves coherent and incoherent processes. Here again, at high energies and strong fields the coherent process will dominate over the incoherent one.

4.1 Beamstrahlung Pair Creation

It is well known that the cross section for incoherent pair creation is

$$\sigma(\gamma e \rightarrow ee^+e^-) \sim \frac{28}{9} \alpha r_e^2 \log\left(\frac{4\omega E}{m^2}\right) \text{cm}^2, \quad (4.1.1)$$

which is a very slowly varying function of the photon energy ω . For TLC, $\gamma = 1 \times 10^6$; the cross section is $\sim 5 \times 10^{-26} \text{cm}^2$ for photons at full energy. The beam parameters for TLC listed in the above Table gives the average number of the beamstrahlung photon per beam particle as $N_\gamma \sim 1.3$. On the other hand, it can be shown¹³⁾ that the effective luminosity for such a cascading process is 1/2 of the original. Thus, the number of e^-e^+ pairs created per bunch crossing can easily be evaluated:

$$N_{e^+e^-}^i = \frac{1}{2} \sigma(\gamma e \rightarrow ee^+e^-) \frac{N_\gamma \mathcal{L}_{ee}}{f_{\text{rep}}} \sim 2 \times 10^5, \quad (4.1.2)$$

where $\mathcal{L}_{ee} = 1.3 \times 10^{33} \text{cm}^{-2} \text{sec}^{-1}$, and $f_{\text{rep}} = 220 \text{sec}^{-1}$ in this design. To be sure, this process provides a non-negligible amount of e^-e^+ pairs.

The rate of photon pair creation in a homogeneous magnetic field has been studied by many people,¹⁵⁾ and has been generalized to inhomogeneous fields by Baier and Katkov.¹⁶⁾ In the asymptotic limits the rate can be expressed as

$$\frac{dI}{dt} = \begin{cases} \frac{3\sqrt{3}}{16\sqrt{2}} \frac{\alpha\Upsilon}{\lambda_c\gamma} e^{-8/3\chi} & , \quad \chi \ll 1 \\ \frac{15}{7} \left(\frac{2}{3}\right)^{1/3} \frac{\Gamma(5/6)}{\Gamma(1/6)} \frac{\alpha\Upsilon}{\lambda_c\gamma} \chi^{-1/3} & , \quad \chi \gg 1 \end{cases} \quad (4.1.3)$$

Here $\chi = \Upsilon\omega/E$ plays the similar role as Υ in the case of beamstrahlung. Notice that χ is independent of the initial particle energy γ , as the process does not care where the photon was originated. Let

$$\frac{dI}{dt} \equiv \frac{\alpha\Upsilon}{\lambda_c\gamma} T(\chi) \quad (4.1.4)$$

To a very good approximation,¹⁷⁾

$$T(\chi) = 0.16\chi^{-1} K_{1/3}^2\left(\frac{4}{3\chi}\right) \quad (4.1.5)$$

for all values of χ .

Integrating over the collision time (again, only half of the e^-e^+ collision time) we have

$$\begin{aligned} I &= \frac{\sqrt{3}}{2} \frac{\sigma_z \alpha \Upsilon}{\lambda_c \gamma} T(\chi) \\ &= \frac{1}{2} n_{cl} T(\chi) \end{aligned} \quad (4.1.6)$$

Next we evaluate the mean value of $T(\chi)$ by weighting over the beamstrahlung spectral function,

$$\frac{dn_b}{d\omega} = \frac{1}{\pi} \frac{\alpha \sigma_z}{\gamma^2} \left\{ \int_y^\infty K_{5/3}(x) dx + \frac{\xi^2 y^2}{1 + \xi y} K_{2/3}(y) \right\} \quad (4.1.7)$$

and

$$\langle T(\Upsilon) \rangle = \int_0^E T(\chi) \frac{dn_b}{d\omega} d\omega \bigg/ \int_0^E \frac{dn_b}{d\omega} d\omega \quad (4.1.8)$$

The total number of e^-e^+ pairs created through this coherent process is therefore

$$N_{e^+e^-}^c = \frac{1}{2} N_\gamma n_{cl} \langle T(\Upsilon) \rangle \quad (4.1.9)$$

A plot of $\langle T(\Upsilon) \rangle$ is shown in Fig. 20, where the solid curve is from the exact form of $dn_b/d\omega$ in Eq. (4.1.7) and the dashed curve corresponds to an asymptotic

expression for $dn_b/d\omega$ at large y . The closeness between the two curves suggests that only the spectrum tip contribute effectively to the coherent pair creation process. From the TLC parameters, $n_{cl} \sim 1.9$, so we find that

$$N_{e^+e^-}^c \sim 5 \times 10^7, \quad (4.1.10)$$

which is much larger than the incoherent process.

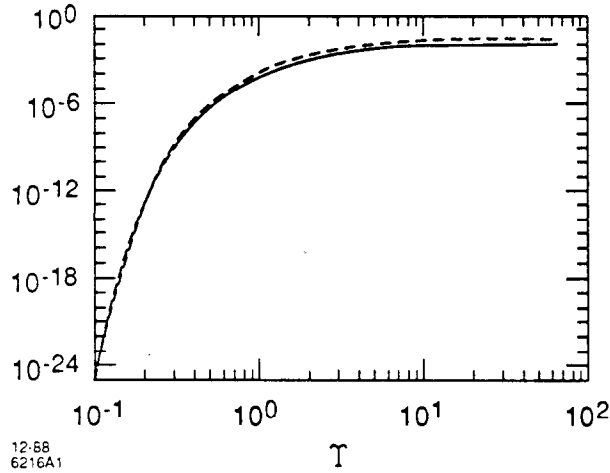


Fig. 20. The function $\langle T(\Upsilon) \rangle$ vs. Υ .

It should be noticed, however, that $\langle T \rangle$ drops exponentially for $\Upsilon \lesssim 1$. Therefore, for next generation linear colliders at the range of 1 TeV, which would typically have $\Upsilon \sim 1$, it would not be at all difficult to redesign the machine such that the coherent process can be entirely suppressed. For the above-mentioned TLC parameters the condition is $\Upsilon \leq 0.3$. This, ironically, is an over-kill since the incoherent process corresponds to $\Upsilon \sim 0.6$, as can be read from Fig. 20.

4.2 Energy Spectrum

Since to a large extent N_γ is of the order unity and quite insensitive to other parameters, and since we usually choose to fix the luminosity in a design, the incoherent e^-e^+ pairs can not be easily suppressed. It is thus important to evaluate the energy spectrum of the pair created e^+ . Assuming constant probability in finding the e^+ at energy $\epsilon E \leq \omega$, the spectrum can be derived to be

$$N_{e^+}(\epsilon) = \frac{7(3/2)^{2/3}}{18\pi^2\Gamma(1/3)} \frac{\alpha^3}{\gamma m} N D_\gamma \Upsilon^{2/3} F(\epsilon, \Upsilon) \quad (4.2.1)$$

The spectral function $F(\epsilon, \Upsilon)$ is plotted in Fig. 21 for $\Upsilon = 0.2$. At the small ϵ limit, $F(\epsilon, \Upsilon) \propto 1/\epsilon$.

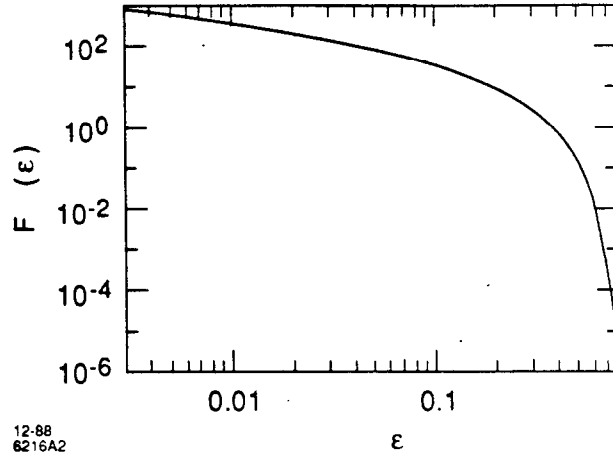


Fig. 21. The spectral function for incoherent pair created e^+ .

The energy spectrum of the pair produced positron from the coherent process can also be obtained from the same basic equation that gives rise to Eq. (4.1.3), without integrating over the final energy. It can be shown that the spectrum is

$$\frac{d^2 I}{d\eta dt} = \frac{1}{\sqrt{3}\pi} \frac{\alpha m}{\gamma} \frac{1}{\varepsilon(\omega - \eta)} \left[\frac{8}{3\chi} \sinh^2 y K_{1/3}(a) + (1 + \tanh^2 y) K_{2/3}(a) \right] \quad (4.2.2)$$

where E is the energy of the positron, and ω the photon energy, both in units of the primary electron energy,

$$\cosh^2 y = \frac{1}{4} \frac{\omega^2}{\eta(\omega - \eta)},$$

and

$$a = \frac{8}{3\chi} \cosh^2 y.$$

Figure 21 is a plot of Eq. (4.2.2) with $\Upsilon = 1.0$, in units of $\alpha m / \sqrt{3}\pi\gamma$. The two curves correspond to beamstrahlung photons at full, i.e., $\chi = 1.0$, and half of the primary e^+e^- beam energy. We see that the spectrum is considerably narrower than the corresponding incoherent process. This is even more so when χ becomes sufficiently less than unity. An intuitive way of understanding this fact is to realize that, although the coherent process at $\Upsilon \sim 1$ has much larger probability than the incoherent one, the equivalent photon energy of the beam-beam field at its range is barely above the invariant mass threshold for pair creation. This is also reflected by the steep exponential decrease of the function $\langle T(\Upsilon) \rangle$. Thus the e^+e^- pair tend to share the initial photon energy evenly, and the damage of the coherent process at the TeV range dose not seem to be too harmful.

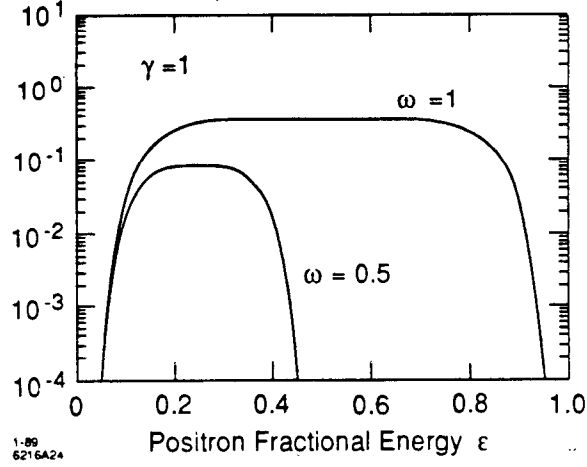


Fig. 22. The positron energy spectrum from coherent pair creation for $\Upsilon = 1$.

4.3 Deflection Angle

Finally, we evaluate the deflection angle of these low-energy positrons by the beam-beam field. As a rough estimation, we assume that the vertical field beyond the beam height extends constantly to a distance equal to the beam width σ_x . It is then easy to show that the deflection angle for the e^+ with energy ϵ is

$$\theta_\epsilon = \begin{cases} \frac{2}{3^{1/4}} \frac{\sigma_x}{\sigma_z} \sqrt{\frac{D_x}{\epsilon}} & , \quad \theta_\epsilon \geq \frac{2}{\sqrt{3}} \theta_d ; \\ 2 \frac{\sigma_x}{\sigma_z} \frac{D_x}{\epsilon} & , \quad \theta_\epsilon \leq \frac{2}{\sqrt{3}} \theta_d . \end{cases} \quad (4.3.1)$$

The deflection angle in the above expression is plotted in Fig. 23. For a 1 GeV e^+ , $\theta_\epsilon \sim 45$ mrad. The information on the transverse momentum can be easily deduced from the above expressions via $p_\perp = \epsilon \theta_\epsilon$.

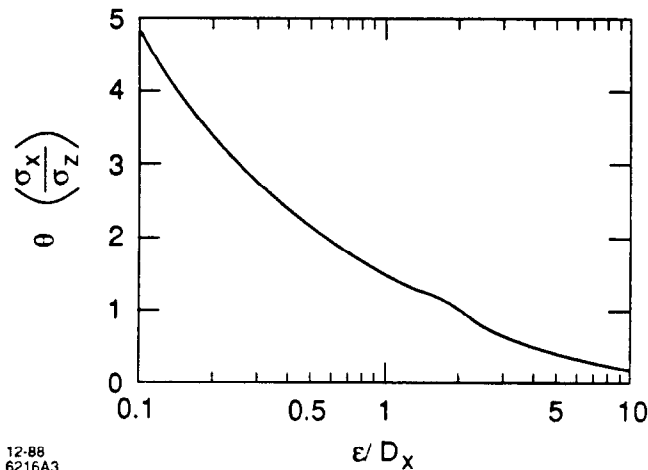


Fig. 23. The deflection angle as a function of e^+ energy.

REFERENCES

1. K. Yokoya, *A Computer Simulation Code for the Beam-Beam Interaction in Linear Colliders*, KEK Report 85-9, October 1985.
2. P. Chen and K. Yokoya, *Disruption Effects from the Interaction of Round e^+e^- Beams*, Phys. Rev. D **38**, 987 (1988).
3. P. Chen and K. Yokoya, *Disruption Effects from the Interaction of flat e^+e^- Beams*, in preparation.
4. W. M. Fawley and E. P. Lee, *Particle in Cell Simulations of Disruption*, in "New Developments in Particle Acceleration Techniques", Orsay 1987, CERN 87-11, ECFA 87/110.
5. R. Holebeek, *Disruption Limits for Linear Colliders*, Nucl. Ins. Meth. 184 (1981).
6. N. A. Solyak, *Collision Effects in Compensated Bunches of Linear Colliders*, Novosibirsk Preprint IYF-88-44, 1988.
7. K. Yokoya and P. Chen, *Multiple Bunch Crossing Instability*, SLAC-PUB-4653, June 1988.
8. Y. H. Chin, *Stability of a Colliding Beam in a Linear Collider*, DESY, January 1987.
9. K. Yokoya and P. Chen, *Depolarization due to Beam-Beam Interaction in Electron-Positron Linear Colliders*, SLAC-PUB-4692, September 1988; and in the *Proceedings for the Eighth International Symposium on High Energy Spin Physics*, 1988.

10. P. Chen and K. Yokoya, *Final Electron Energy Spectrum and Maximum Deflection Angle under Beamstrahlung*, in preparation.
11. R. B. Palmer, *Interdependence of Parameters for TeV Linear Colliders*. SLAC-PUB-4295, April 1987; and SLAC-AAS-39, November 1988.
12. P. Chen, *Review of Beam-Beam Interaction*, summary talk given at the International Workshop on the Next Generation Linear Colliders. November 28-December 9, 1988, SLAC, Stanford; and P. Chen, *Disruption, Beamstrahlung and Beamstrahlung Pair Creation*, SLAC-PUB-4822, December 1988; to appear in the Proceedings of the DPF Summer Study Snowmass '88, High Energy Physics in the 1990's.
13. M. S. Zolotarev, E. A. Kuraev and V. G. Serbo, *Estimates of Electromagnetic Background Processes for the VLEPP Project*, Inst. Yadernoi Fiziki. Preprint 81-63, 1981; English translation SLAC TRANS-0227, 1987.
14. I. F. Ginzburg, G. L. Kotkin, V. G. Serbo and V. I. Telnov, *Colliding γe and $\gamma\gamma$ Beams Based on the Single-Pass Accelerators*, Inst. Nucl. Phys. (Novosibirsk) Preprint 81-102, 1981.
15. See, for example, W. Y. Tsai and T. Erber, Phys. Rev. D **10**, 492, 1974; and references therein.
16. V. N. Baier and V. M. Katkov, Soviet Phys. JETP **26**, 854, 1968.
17. T. Erber, Rev. Mod. Phys. **38**, 626, 1966.